Effects of Thermal Non-Equilibrium During Transition to Turbulence of a High Enthalpy Free Shear Layer

A. Musawi[1] and N. D. Sandham[1]
University of Southampton, Boldrewood Innovation Campus, Burgess Rd, Southampton SO16 7QF

(Dated: 28 December 2025)

Under the high-enthalpy conditions encountered in hypersonic flight, non-equilibrium effects from vibrational excitation and chemical reactions complicate the prediction of transition to turbulence and the developed turbulent state. This study assesses the impact of thermal non-equilibrium on turbulence properties for a canonical compressible mixing layer and evaluates the influence of vibration modelling approaches, particularly the difference between using a single vibration energy equation versus separate equations for each molecular species. Preliminary two-dimensional simulations reveal two distinct patterns of thermal non-equilibrium dependent on temperature: one characterised by thermally hot vortex cores and the other by a combination of hot and cold regions around developing vortices. Chemical non-equilibrium effects are minimal, as the timescales of chemical reactions are significantly shorter than those of the flow. The importance of intermolecular vibration modelling is highlighted by comparing results from a single fully-coupled vibration equation with an artificial limiting case of three separate vibration equations without intermolecular coupling. Three-dimensional direct numerical simulations show trends consistent with the two-dimensional cases, with hot vortex cores forming in the low-temperature case and more complex hot–cold patterns surrounding vortex tubes when thermal and flow timescales are comparable. At later stages of breakdown and turbulence decay, differences between cases are enhanced by amplification of small perturbations, i.e. non-linear flow dynamics that result in symmetry breaking, and cannot be attributed directly to non-equilibrium effects. Nevertheless, turbulence statistics show that increased thermal non-equilibrium is correlated with increased translational temperature fluctuations, related to variation in mean translational temperature across the shear layer.

I. INTRODUCTION

Driven by the growing interest in hypersonic flight, considerable advancements have been made in understanding high enthalpy flow regimes. Nevertheless, fundamental gaps remain in the understanding of interactions between fluid flow and high-enthalpy phenomena, particularly concerning the coexistence of turbulence with chemical and thermal processes. Moreover, many of the approximations and assumptions employed in modelling high-enthalpy effects have not been subjected to thorough scrutiny or validation.

Relatively few studies to date have exploited developments in high-performance computing to apply direct numerical simulation (DNS) to non-equilibrium phenomena in turbulent flow regimes[1]. Examples of this approach include investigations of thermo-chemical non-equilibrium boundary layers[2] using a multi-temperature framework, demonstrating that turbulence–chemistry interactions result in compositional variation across the boundary layer and that chemical non-equilibrium has a stabilising effect on secondary instabilities[3]. Other studies have shown that turbulence–thermal interactions can sustain thermal non-equilibrium through turbulent mixing[4,5]. Further investigations have explored the effects of high-enthalpy conditions on decaying isotropic turbulence using DNS[6,7]. Furthermore, research on vibrational relaxation effects has highlighted both the damping of temperature fluctuations and the role of acoustic waves in generating fluctuations[8]. A more recent study[9] investigated turbulent thermal non-equilibrium flow, demonstrating the coupling between turbulence and vibrational relaxation using a state-specific model. These DNS simulations reveal that translational energy develops through compressible fluid mechanics, while vibrational energy evolves on its own relaxation timescale, thereby triggering local vibrational non-equilibrium.

The two-stream planar mixing layer is a canonical configuration to study transition and turbulence in high-speed shear flows. Mixing layers have been extensively used to develop and test turbulence models, to analyse the structure and dynamics of organised motion in turbulent flows, and to complement experimental investigations[10]. Examples include DNS of incompressible plane mixing layers, showing non-linear effects following the Kelvin–Helmholtz instability[11] and the development towards self-similar shear layer growth[12]. Further work has examined the effect of compressibility on mixing layers, analysing reductions in growth rates through statistical methods across a wide range of convective Mach numbers[13], and linking this reduction to the pressure–strain term in the turbulence stress transport equations. The influence of large-scale structure dynamics on the transport of a conserved scalar and the associated concentration profiles across shear layers has also been studied[14]. More recent investigations include studies of compressibility effects on statistics and structures near the interfaces of high- and low-speed large-scale structures[15], analyses of structural evolution and turbulence statistics in spatially developing mixing layers[16] concluding that ring-like vortices significantly promote mixing and extend the transition stage, and research on the role of bulk viscosity in chemically reacting compressible shear layers developing through shock waves[17].

Given the influence of high-enthalpy effects on flow characteristics and the pivotal role of mixing layer simulations in advancing the understanding of compressible turbulent flows, it is evident that further studies of the impact of thermo-chemical non-equilibrium on turbulence within

a DNS framework are needed. Furthermore, careful consideration must be given to the assumptions and approximations employed in modelling high-enthalpy effects, along with their physical implications in a non-equilibrium context. The primary objective of this study is to evaluate the extent to which thermal non-equilibrium influences turbulence properties in a compressible mixing layer configuration. A secondary objective is to assess how certain modelling approximations affect the results. The temperature range considered extends up to $6000\,K$, such that ionisation effects are not included. Sections II and III review the formulation and modelling assumptions for non-equilibrium flow. Section IV presents the mixing layer problem, including symmetry-breaking characteristics. Section V reports the results for two- and three-dimensional cases.

II. GOVERNING EQUATIONS

The governing equations for thermo-chemical non-equilibrium simulations consist of the continuity, momentum, vibrational energy, and total energy conservation equations[18]. The species equations account for chemical reactions within the mixture, as well as thermal energy exchange between the rotational–translational and vibrational modes. A two-temperature representation of the energy modes is employed, in which the electronic mode is neglected and only the five neutral species of air are considered. The full set of conservation equations is given by

$$\frac{\partial}{\partial t}\rho_s + \frac{\partial}{\partial x_j}\rho_s u_j = \frac{\partial}{\partial x_j}\left(\rho D_s \frac{\partial X_s}{\partial x_j}\right) + \dot{\omega}_s + D_s^{cor} \tag{1}$$

$$\frac{\partial}{\partial t}\rho u_i + \frac{\partial}{\partial x_j}\rho u_i u_j = -\frac{\partial p}{\partial x_i} + \frac{\partial}{\partial x_j}\left[\mu\left(\frac{\partial u_i}{\partial x_j} + \frac{\partial u_j}{\partial x_i}\right) - \frac{2}{3}\mu\frac{\partial u_k}{\partial x_k}\delta_{ij}\right] \tag{2}$$

$$\frac{\partial}{\partial t}\rho e_v + \frac{\partial}{\partial x_j}\rho e_v u_j = \frac{\partial}{\partial x_j}\left(\kappa_v \frac{\partial T_v}{\partial x_j}\right) + \frac{\partial}{\partial x_j}\left(\rho \sum_{s=1}^{5} e_{v,s} D_s \frac{\partial X_s}{\partial x_j}\right) + \sum_{s=mol} \rho_s \frac{(e^*_{v,s} - e_{v,s})}{\tau_s} + \sum_{s=mol} \dot{\omega}_s e_{v,s} \tag{3}$$

$$\frac{\partial}{\partial t}\rho E + \frac{\partial}{\partial x_j}\rho H u_j = \frac{\partial}{\partial x_j}\left(\kappa_{tr}\frac{\partial T}{\partial x_j} + \kappa_v \frac{\partial T_v}{\partial x_j}\right) + \frac{\partial}{\partial x_j}\left(\rho \sum_{s=1}^{5} h_s D_s \frac{\partial X_s}{\partial x_j}\right) + \frac{\partial}{\partial x_j}\left[u_i \mu\left(\frac{\partial u_i}{\partial x_j} + \frac{\partial u_j}{\partial x_i}\right) - \frac{2}{3}u_i\mu\frac{\partial u_k}{\partial x_k}\delta_{ij}\right] \tag{4}$$

where s refers to the species (O, O_2, N, N_2, NO); ρ is the density ($\mathrm{kg\,m^{-3}}$); t is time (s); u is the velocity ($\mathrm{m\,s^{-1}}$); D_s is the species diffusion coefficient ($\mathrm{m^2\,s^{-1}}$); X_s is the mole fraction; $\dot{\omega}_s$ is the mass production rate ($\mathrm{kg\,m^{-3}\,s^{-1}}$); p is the pressure (Pa); μ is the mixture viscosity ($\mathrm{kg\,m^{-1}\,s^{-1}}$); δ_{ij} is the Kronecker delta; e_v is the vibrational energy ($\mathrm{J\,kg^{-1}}$); κ_v is the vibrational component of the thermal conductivity ($\mathrm{W\,m^{-1}\,K^{-1}}$); T_v is the vibrational temperature (K); e_v^* is the instantaneous equilibrium vibrational energy ($\mathrm{J\,kg^{-1}}$); E is the specific total energy ($\mathrm{J\,kg^{-1}}$); H is the specific total enthalpy ($\mathrm{J\,kg^{-1}}$); κ_{tr} is the rotational–translational contribution to the thermal conductivity ($\mathrm{W\,m^{-1}\,K^{-1}}$); h_s is the species specific enthalpy ($\mathrm{J\,kg^{-1}}$); and subscript $i = 1,2,3$ indexes the x,y,z directions respectively. The governing equations are based on three main assumptions[19]. First, the flow is assumed to be in a continuum state. Second, a multi-temperature model is used, where the energy modes are represented by their respective temperatures, and the rotational and translational modes are assumed to be coupled and represented by the translational temperature T. Third, the vibrational energy is represented by a single vibrational temperature T_v, with the vibrational energy levels assumed to follow a Boltzmann distribution.

A. Conservation of Species Vibrational Energy

The conservation of vibrational energy, expressed in Eq. 3, assumes fully coupled molecular species, i.e. the vibrational–vibrational (V-V) energy exchange rate is effectively infinite. Consequently, the total vibrational energy is represented by a single conservation equation, with only the vibrational-translational (V-T) energy exchange appearing explicitly. This form is widely used in numerical simulations[3–5,18,20–22]. For a more detailed representation, the transport of vibrational energy can be formulated separately for each molecular species as

$$\frac{\partial}{\partial t}\rho_s e_{v,s} + \frac{\partial}{\partial x_j}\rho_s e_{v,s} u_j = \frac{\partial}{\partial x_j}\left(\kappa_{v,s}\frac{\partial T_v}{\partial x_j}\right) + \frac{\partial}{\partial x_j}\left(\rho e_{v,s} D_s \frac{\partial X_s}{\partial x_j}\right) + \frac{\rho_s (e^*_{v,s} - e_{v,s})}{\tau_s} + \dot{\omega}_s e_{v,s} \quad . \tag{5}$$

Equation 5 represents the original form from which Eq. 3 was derived, as presented in Ref. 19 and later referenced in Ref. 18. When the vibrational modes are split by species, in addition to the energy exchange between rotational–translational and vibrational modes,

inter-species vibrational energy exchange should also be considered. Since the modelling requirements are still under investigation[23], the present study is restricted to two cases: (i) full coupling between molecular relaxations, resulting in a single vibrational energy equation; and (ii) no vibrational–vibrational energy exchange, resulting in a system of three separate vibrational energy equations. While the first case can be physically justified, the second formulation is unlikely to be achieved in practice. As shown in Ref. 24, the inclusion of V-V relaxation can be significant, increasing the overall vibrational relaxation rate of N_2 by approximately a factor of three, although it becomes slower for O_2 . It is, however, known that V-V relaxation rates can be comparable to or even lower than V-T relaxation rates at very low pressures[25–28] or at very high temperatures. In this context, the two models considered here represent limiting cases intended to assess the influence of molecular coupling.

B. Energy Equation

The total energy per unit mass of a mixture can be expressed as the sum of separate components[29]

$$E/\rho = \sum e_{t,s} + \sum e_{r,s} + \sum e_{v,s} + e_e + \sum e_{el,s} + \frac{1}{2}u_i u_i + \sum \frac{\rho_s h_s^\circ}{\rho} \,. \quad (6)$$

In general, this consists of translational, rotational, vibrational, electron translational, electronic, kinetic, and chemical components. Given that the temperature range considered in this study remains well below 9000 K, ionisation can be neglected with reasonable accuracy, allowing both electron translational and electronic energies to be neglected. Furthermore, since rotational modes are fully excited at temperatures above a few K (approximately 2–3 K for air species), the rotational mode can be considered fully excited and can be assumed to be in equilibrium with the translational mode[30]. Therefore, these two modes can be represented by a single temperature. The combined translational–rotational energy can be expressed as

$$\rho e_{tr} = \sum \frac{3}{2}\rho_s R_s T_t + \rho_s R_s T_r = \mathscr{R} T \left[\sum_{s=atom} \frac{3}{2}\frac{\rho_s}{M_s} + \sum_{s=mol} \frac{5}{2}\frac{\rho_s}{M_s} \right] \quad , \quad (7)$$

where ρ_s is the species density, R_s is the species gas constant, T_t is the translational temperature, T_r is the rotational temperature, $\mathscr{R}$ is the universal gas constant, and M_s is the species molecular mass. Here, *mol* refers to the molecules N_2, O_2 and NO, and *atom* refers to the atoms N and O. The symbol T denotes the rotational–translational temperature representing the coupled rotational and translational modes. The vibrational energy is modelled with a simple harmonic oscillator at the vibrational temperature

$$\rho e_v = \sum_{s=mol} \rho_s e_{v,s} = \sum_{s=mol} \rho_s \frac{\mathscr{R}}{M_s} \frac{\theta_{v,s}}{e^{\theta_{v,s}/T_{v,s}} - 1} \quad , \quad (8)$$

where $\theta_{v,s}$ is the characteristic vibrational temperature for species s, and $T_{v,s}$ is the species vibrational temperature. Equation 8 adopts the rigid-rotor and harmonic-oscillator (RRHO) models: diatomic bond lengths are treated as fixed for rotations (rigid rotor) and vibrational motion is modelled as a simple harmonic oscillator. The harmonic oscillator (HO) model is applied, assuming symmetric interatomic interactions between repulsive and attractive forces. Although anharmonic effects exist in reality, the HO model remains accurate at lower temperatures, where higher vibrational states are less populated. Indeed, comparisons of this model for five-species air with thermo-chemical data, such as NASA-9[31], show only slight deviations starting at approximately 8000 K.

C. Transport Properties

An accurate description of the transport of momentum, energy, and mass is essential to characterise the flow environment, especially for thermo-chemical non-equilibrium flows. In the physical modelling of transport properties, mass and momentum fluxes (corresponding to diffusion and viscosity, respectively) are not influenced by the presence of internal modes. However, the energy flux, via the thermal conductivity, accounts for contributions from both translational and internal modes[32]. According to classical kinetic theory, mass transport (diffusion) arises from concentration gradients, while energy transport (thermal conductivity) is driven by temperature gradients[32]. In this study, cross-coupling effects i.e. mass transport due to temperature gradients (Soret effect) and energy transport due to concentration gradients (Dufour effect) are neglected.

The work of Chapman and Enskog enabled the theoretical derivation of complete equations for transport properties[32,33]. However, for multi-component gas mixtures, the full expressions are complex and computationally expensive. Consequently, approximations are typically employed to reduce costs, such as mixing rules. Comparative studies have evaluated various methods, including the Yos–Gupta mixing rule[34–36], the Wilke mixing rule[37], and the Armaly–Sutton mixing rule[38] for calculating viscosity and thermal conductivity. These studies concluded that the Yos–Gupta method offers advantages in accuracy and computational efficiency from 200 K to 20,000 K for non-ionised regimes[39,40]. Nevertheless, even the Yos–Gupta method can become computationally intensive for scale-resolved simulations, such as direct numerical simulation (DNS).

For this study, a more efficient formulation for viscosity and thermal conductivity is used[41], optimised against the Yos–Gupta model and expressed in the form

$$\mu, \kappa_{tr} = \frac{\sum\limits_{s=atom} 15X_s + \sum\limits_{s=mol} 30X_s}{P(a,b,c,d)\sum\limits_{s=atom} X_s + P(e,f,g,h)\sum\limits_{s=mol} X_s} - \Phi, \quad (9)$$

with

$$P(A,B,C,D) = \left| A + BT^2 + C\ln T + \frac{D}{T} \right|, \tag{10}$$

where A, B, C, and D vary for μ and κ_{tr} and are given in Appendix A. For all cases, the third implementation specified by Ref. 41 is used, assuming strong non-equilibrium conditions, with a correction factor Φ defined as

$$\Phi = \left| 2.03\,(T - T_v)\,T \times 10^{-10} \right| \tag{11}$$

for thermal conductivity and 0 for viscosity. In addition, species and total vibrational thermal conductivities are expressed as

$$\kappa_{v_s} = \left| X_s \left(a_s + b_s T_d + c_s T_d^2 + d_s T_d^3 + e_s T_d^4 + f_s T_d^5 + g_s T_d^6 \right) \right|, \tag{12}$$

$$\kappa_v = \sum_{s=mol} \kappa_{v_s}. \tag{13}$$

The coefficients in Eq. 12 are provided in Appendix A. The models selected for viscosity and thermal conductivity are expressed in terms of species mole fractions and vibrational temperature, thereby enabling the incorporation of thermo-chemical non-equilibrium effects into the transport properties. This formulation has been evaluated and benchmarked against various models[41], showing strong agreement with the Yos–Gupta model.

Similar to viscosity and thermal conductivity, the full formulation of diffusion in gas mixtures[32] is too computationally intensive for practical use. For modelling mass flux, an alternative to the full Chapman–Enskog formulation is the self-consistent effective binary diffusion (SCEBD) approximation[42], where the diffusion velocity of species s is treated as that of a binary mixture relative to a composite of all other species. Using this definition with Fick's law, the diffusion velocity yields the form in Eq. 1. In this study the mole-fraction form is utilised, with the effective diffusion coefficient defined as[43]

$$D_s = \frac{\gamma_t^2 M_s (1 - M_s \gamma_s)}{\sum_{m \neq s} \gamma_m / D_{sm}} \quad , \tag{14}$$

where γ_s is the molar concentration of species s, and γ_t is the total molar concentration defined as

$$\gamma_s = \frac{\rho_s}{\rho M_s} \quad , \tag{15}$$

$$\gamma_t = \sum \gamma_s \quad , \tag{16}$$

and D_{sm} is the binary diffusion coefficient expressed in polynomial form by Ref. 36 as

$$D_{sm} = \frac{kT}{p\,\Delta_{sm}^{(1)}} = \frac{p\,\exp(D_d)}{1.01325 \times 10^9}\; T^{A_d \ln^2 T + B_d \ln T + C_d} \quad , \tag{17}$$

where k is the Boltzmann constant, p is the pressure, $\Delta_{sm}^{(1)}$ is the collision integral, and the coefficients A_d, B_d, C_d, and D_d are given in Ref. 36. In this model, the sum of diffusion mass fluxes does not inherently equal zero; hence a correction factor is widely adopted[3,22,44,45]. The correction term is defined as[46]

$$D_s^{cor} = \rho_s \sum D_s \frac{\partial X_s}{\partial x_j} \quad , \tag{18}$$

where D_s is the species diffusion coefficient. This correction term is not needed when a constant Schmidt number is used to model diffusion.

Recent research on the impact of modelling bulk (volume) viscosity[17,47–50] shows that the effect for air is small. Given the limited dilatational influences in mixing-layer simulations at the higher Mach numbers studied here[13,51], Stokes' hypothesis is assumed applicable and bulk viscosity is not included.

D. Vibrational Temperature

With the expressions in the governing equations and the later requirements for chemical models, a single vibrational temperature is necessary. However, since the RRHO expression for vibrational energy contains species-specific variables, either an estimate can be made, using

$$T_{v,s} = \frac{\theta_s}{\ln\left(1 + \frac{\theta_s R_s}{e_{v,s}}\right)} \quad \text{and} \quad T_v = \frac{\bar{\theta}}{\ln\left(1 + \frac{\bar{\theta}\bar{R}}{e_v}\right)} \quad ,$$

where $\bar{\theta}$ and $\bar{R}$ are the weighted averages of the characteristic vibrational temperature and gas constant, respectively; or the vibrational temperature can be calculated iteratively. In the current work, a Newton–Raphson procedure is used to find the overall T_v

$$T_v^{n+1} = T_v^n + \frac{(\rho e_v - \sum \rho_s e_{v,s})}{\sum \rho_s \frac{\partial e_{v,s}}{\partial T_v}} \quad , \tag{19}$$

where the superscript n is the iteration counter, and

$$\frac{\partial e_{v,s}}{\partial T_v} = \frac{\theta_s^2 \mathscr{R}}{T_v^2 \hat{M}_s} \frac{e^{\theta_s/T_v}}{\left(e^{\theta_s/T_v} - 1\right)^2} \quad . \tag{20}$$

E. Other Relations

For the gas mixture, Dalton's law of partial pressure is assumed where the total pressure can be expressed as

$$p = \sum \rho_s \frac{\mathscr{R}}{M_s} T \quad . \tag{21}$$

From statistical thermodynamics, following the expression for total energy (Equation 6) and hence enthalpy, the frozen species specific heat (C_{p_s}) can be expressed as

$$C_{p_s} = \frac{3}{2}\frac{\mathscr{R}}{M_s} + \frac{\mathscr{R}}{M_s} + \frac{(\theta_s/T_v)^2 e^{\theta_s/T_v}}{\left(e^{\theta_s/T_v} - 1\right)^2}\frac{\mathscr{R}}{M_s} + \frac{\mathscr{R}}{M_s} \quad . \tag{22}$$

TABLE I: Properties used for each species[31,52].

		O	O_2	N	N_2	NO
M	(kg/mol)	0.016	0.032	0.014	0.028	0.030
θ_s	(K)	-	2270	-	3390	2740
h°	(MJ/kg)	15.575	0	33.764	0	5.704

The frozen mixture specific heat can then be derived by

$$C_p = \sum_s Y_s C_{p_s} \quad , \tag{23}$$

where Y_s is the mass fraction. Species enthalpy and specific heat can also be expressed using tabulated data in polynomial form[31,36].

The enthalpy of formation at the reference temperature and other thermodynamic properties used in this study are summarised in Table I.

III. THERMO-CHEMICAL MODEL

A. Chemical Kinteic Model

Following the introduction of Park's two-temperature model, several variations of the formulation have appeared[53–58], alongside publications that have presented updated rates for specific reactions[59]. The variations arise primarily from (i) differences in the equilibrium composition of air, which depend on the evaluation points used for determining equilibrium constants from stoichiometric data, and (ii) revisions to reaction rate coefficients based on newly available experimental or empirical data.

It should be noted that several reaction rates within Park's models are still based on experimental data obtained over three decades ago. Consequently, various studies have updated these coefficients in line with more recent measurements or derived data[60,61]. The most frequently cited versions of Park's model are found in Refs. 56 and 58, with additional reference to Ref. 55 due to its association with the publication of Ref. 18. In this work, Park's multi-temperature chemical model is employed as described in Refs. 56 and 58, where the latter provides a reaction (the dissociation of nitric oxide [NO] into atomic nitrogen [N] and atomic oxygen [O]) omitted from the former.

The five-species air model considered here consists of O, O_2, N, N_2, NO and comprises five reactions:

$$\begin{aligned} N_2 + M &\longleftrightarrow 2N + M \\ O_2 + M &\longleftrightarrow 2O + M \\ NO + M &\longleftrightarrow N + O + M \\ N_2 + O &\longleftrightarrow NO + N \\ NO + O &\longleftrightarrow O_2 + N \end{aligned} \tag{24}$$

1. Equilibrium Constant

Among the multi-temperature (MT) models discussed in papers such as Refs. 18, 58, and 62, the equilibrium constant is expressed as a function of a polynomial with a given set of coefficients. Depending on the temperature points evaluated when referring to the stoichiometric data and the form of the equation, the coefficients differ and hence the derived equilibrium state of the mixture using the equations will be different.

Another method for evaluating the equilibrium constant is to use thermo-chemical databases such as the NASA-9 polynomials[31] by computing the Gibbs function for each reaction. The Gibbs function, expressed in terms of enthalpy and entropy, can be obtained from those polynomials. While the NASA-9 approach is generally more accurate, Park's formulation uses fewer coefficients and has a simpler functional form. Additionally, NASA-9 coefficients are split across three temperature ranges (200 K–1000 K, 1000 K–6000 K, and 6000 K–20,000 K), requiring storage of three coefficient sets to cover, for example, 300 K–9000 K, as opposed to a single set.

In the present work we represent the equilibrium constant by

$$\ln(K_c) = a_i T^{-1.5} + b_i T^{-1} + c_i + d_i \ln T + e_i T + f_i T^2, \tag{25}$$

aligning with cgs-based units used for the chemical model defined below. The NASA-9 database[31] was used to optimise the constants, where the subscript i indicates the reaction, and the coefficients for each reaction are given in Table II.

2. Chemical Reaction

The source term for each species in a non-equilibrium state can be expressed as the sum of its reaction rates. For consistency with coefficients given in most literature, the chemical reaction formulation given in this section is done so in cgs units. The rate of production of species s per unit volume is

$$\dot{\omega}_s = M_s \sum (\beta_{s,r} - \alpha_{s,r})(R_{f,r} - R_{b,r}) \quad , \tag{26}$$

where $\beta_{s,r}$ and $\alpha_{s,r}$ are the stoichiometric coefficients for products and reactants, respectively, and $R_{f,r}$ and $R_{b,r}$ are the forward and backward reaction rates, and M_s is in grams. The reaction rates are defined as

$$R_{f,r} = 1000 \left[k_{f,r} \prod_{s=1}^{5} (0.001 \rho_s / M_s)^{\alpha_{s,r}} \right] \quad , \tag{27}$$

$$R_{b,r} = 1000 \left[k_{b,r} \prod_{s=1}^{5} (0.001 \rho_s / M_s)^{\beta_{s,r}} \right] \quad , \tag{28}$$

where $k_{f,r}$ and $k_{b,r}$ are the forward and backward rate coefficients and M_s is in grams. The coefficients are given in cgs-based units; the factors 1000 and 0.001 convert

TABLE II: Coefficients for equilibrium constant defined as Eq. 25.

Reaction (i)	a	b	c	d	e	f
$O_2 + M \leftrightarrow 2O + M$	2.09180e+03	-1.13450e+05	3.76460e+00	1.56100e+00	-3.30080e-04	1.83680e-08
$N_2 + M \leftrightarrow 2N + M$	5.02970e+03	-7.59480e+04	5.16380e+00	1.18180e+00	-2.21420e-04	1.17870e-08
$NO + M \leftrightarrow N + O + M$	6.27520e+03	-6.01790e+04	7.48960e+00	1.09320e+00	-2.14740e-04	7.29820e-09
$NO + O \leftrightarrow N + O_2$	-2.93790e+03	-3.74970e+04	-1.39920e+00	3.79240e-01	-1.08650e-04	6.58020e-09
$N_2 + O \leftrightarrow N + NO$	-1.24550e+03	-1.57690e+04	-2.32590e+00	8.85260e-02	-6.68590e-06	4.48930e-09

to SI-consistent units. In Park's model the forward rate coefficients follow an Arrhenius form:

$$k_{r_f} = C T_a^n \exp(-T_f/T_a) \quad , \tag{29}$$

where T_a is the controlling (effective) temperature, C is the pre-exponential constant (in $\mathrm{cm}^3/\mathrm{mol}$ for bimolecular reactions), n is the temperature exponent, and T_f is the activation temperature.

When compared to experimental data, the observed times to reach equilibrium were longer than those predicted by conventional theories. Hence, the multi-temperature model presented by Ref. 63 assumes a coupling between the two temperatures (ro-translational and vibrational) for the chemical reactions, in order to account for the influence of vibrational relaxation on the chemical reactions. The relation between the two temperatures is presented as

$$T_a = T^{\,\lambda}\, T_v^{\,1-\lambda} \quad , \tag{30}$$

where λ is typically between 0.5 and 0.7[56]. In this work, λ is set to 0.5. The backward rate is obtained from the forward rate and the equilibrium constant as

$$k_{r_b} = \frac{k_{r_f}(T)}{K_c} \quad . \tag{31}$$

The forward rate used in Eq. 31 is evaluated at the translational temperature (rather than the two-temperature blend). Details of temperature choices and extensions including ionisation are discussed elsewhere[53,64].

B. Thermal Kinetic Model

The foundation of the multi-temperature method for thermal non-equilibrium is the Landau–Teller expression[65], which underpins models such as Millikan–White[66], widely used in computational analyses. The following paragraphs provide more detail on the implementation of this approach.

1. Relaxation Time

The formulation in Ref. 66, including corrected forms[62], is a standard source for vibrational relaxation times. The energy exchange between the translational and vibrational modes is characterised by a vibrational relaxation time τ_s. A semi-empirical model valid over 300 K–8000 K is given by[66]

$$\tilde{p}\tau^{MW} = \exp[\mathrm{A}(T^{-1/3} - \mathrm{B}) - 18.42] \quad , \tag{32}$$

in atm·s, where $\tilde{p} = p/101325$, and A ($= \mu^m \theta^n$) and B include constants m and n that can be approximated via

$$A = 0.00116\mu^{0.5}\theta^{1.333} \quad ,$$
$$B = 0.015\mu^{1/4} \quad ,$$

where μ is the reduced mass of the colliding pair ($\mu_{sj} = M_s M_j/(M_s + M_j)$) and θ is the characteristic vibrational temperature. Updated coefficients for the Millikan–White relaxation were given in Ref. 56. The coefficeints used in this study are those given by Ref. 18 and are given in Appendix C.

As collisions occur with a mixture of heavy particles (including the species s), an average over collision partners is used to obtain the molecular relaxation time τ_m from Eq. 32. The most common approach[4,5,19,62,67] is a weighted harmonic average such that

$$\tau_m^{MW} = \frac{\sum X_s}{\sum X_s/\,\tau_s^{MW}} \quad , \tag{33}$$

with X_s being the mole fraction and m subscript representing the molecules. As an approximation to reduce computational processing another method[18] consists of deriving a single overall relaxation time by performing a weighted arithmetic average between the species and a harmonic averaging between the molecules

$$\tau_m^{MW} = \frac{\sum X_s\,\tau_s^{MW}}{\sum X_s} \quad \text{and} \quad \tau = \frac{\sum X_m}{\sum X_m/\,\tau_m^{MW}} \quad . \tag{34}$$

Within a single vibrational energy conservation equation, where molecular species are assumed to be mutually coupled, the use of a single effective relaxation time is consistent with the other modelling assumptions and produces little difference relative to Eq. 33. As relaxation is a rate process, harmonic averaging is the appropriate form when rates are combined. In this study, the vibrational relaxation times for the multi-e_v formulation are given by Eq. 33, while for simulations with a single-e_v formulation, Eq. 34 is used.

A correction to the Millikan–White formulation was proposed in Ref. 62 to avoid excessively large values above 8000 K. The impact of this correction was assessed for the present study and found to be negligible over the temperatures used (up to 6000 K), and was therefore not included.

2. Molecular Production/Depletion

The term $\dot{\omega}_s e_{v_s}$ in Eq. 3, with $s = mol$, represents the creation or destruction of vibrational energy within each species due to high vibrational quantum numbers, where $\dot{\omega}_s$ is the production rate of molecule s (from the reaction system) and e_{v_s} is the vibrational energy per unit mass of the molecules. This representation, which is appropriate for non-preferential dissociation, is adopted in the present work. Alternative forms suitable for preferential dissociation are available[18,59].

3. Thermal Equilibrium

To evaluate the influence of non-equilibrium effects, a corresponding simulation is performed under the assumption of thermal equilibrium. In this case, all internal energy modes are represented by a single temperature, including the vibrational contribution. As the vibrational temperature reduces to a function of the translational temperature, the separate vibrational energy conservation equation is no longer required. However, directly recovering the translational temperature from the total energy (Eq. 6) is less straightforward because of the vibrational terms embedded within it. To address this, a Newton–Raphson iterative method is employed to compute the translational temperature, given by

$$f(T) = \frac{\rho E - \frac{1}{2}u_i u_i - \mathscr{R}\sum_{mol}\frac{\rho_s\theta_s}{M_s(\exp^{\theta_s/T}-1)} - \sum\frac{\rho_s h_s^\circ}{\rho}}{\beta} - T, \quad (35)$$

$$f'(T) = -\frac{\mathscr{R}}{T^2\beta}\sum_{mol}\frac{\rho_s\theta_s^2 e^{\theta_s/T}}{M_s(e^{\theta_s/T}-1)^2} - 1 \quad , \quad (36)$$

$$T^{n+1} = T^n - \frac{f(T^n)}{f'(T^n)} \quad , \quad (37)$$

where n is the iteration index and

$$\beta = \mathscr{R}\left[\sum_{s=atom}\frac{3}{2}\frac{\rho_s}{M_s} + \sum_{s=mol}\frac{5}{2}\frac{\rho_s}{M_s}\right] \quad . \quad (38)$$

This results in a thermal equilibrium state throughout the simulation, while also considering the contribution from internal modes.

IV. MIXING LAYER

A two-stream mixing layer is one of the simplest configurations for studying inhomogeneous shear flow without walls and has been widely used to investigate the development of compressible turbulence in high-speed free shear flows[68]. Similar behaviour is observed among plane, annular, and certain jet flows when considering mean and turbulence characteristics[69]. In mixing layers, transition to turbulence begins with a primary instability of Kelvin–Helmholtz type, owing to the inflectional nature of the velocity profile. Mixing layers may be configured as either spatial, corresponding to the laboratory frame of reference, or temporal, where the initial condition consists of two streams moving in opposite directions. Despite some differences between the two, such as asymmetric entrainment in the spatial case, the main mechanisms of instability, breakdown, entrainment, and the stabilising effect of compressibility remain the same. Ref. 12 compared DNS of temporally and spatially evolving mixing layers and reported no qualitative and, in most cases, no quantitative differences.

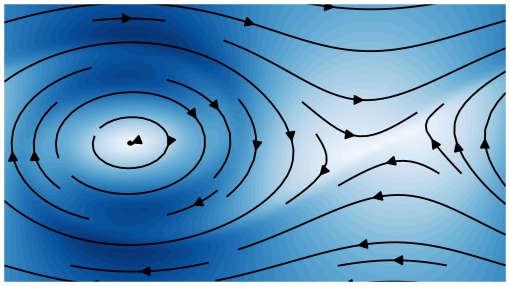

FIG. 1: Instantaneous streamlines (black lines) in a 2D mixing layer superimposed on colour contours showing velocity magnitude, with white indicating zero velocity.

Figure 1 shows a schematic of a temporally evolving two-dimensional mixing layer, where the colour contours represent velocity magnitude. The bright region on the left marks the vortex core, while that on the right indicates the stagnation point. In a compressible flow, there is an increase in density, pressure and temperature along the streamline that approaches the stagnation point, with the opposite effect for streamlines moving away from the stagnation point and subsequently entrained into the vortex core. This conceptual picture will be useful when discussing the role of thermo-chemical non-equilibrium.

A. Numerical Setup

The governing equations were discretised using finite differences. Both spatial and temporal discretisation were implemented in OpenSBLI[70,71]. Spatial derivatives were approximated with a fourth-order central difference scheme:

$$\frac{\partial f}{\partial x} = \frac{-f_{i+2} + 8f_{i+1} - 8f_i - 1 + f_{i-2}}{12\Delta x} \quad . \quad (39)$$

Time advancement employed a fourth-order Runge–Kutta (RK) scheme.

For visualisation, a passive scalar was introduced, governed by[72]

$$\frac{\partial(\rho f)}{\partial t} = \frac{\partial(\rho f u_j)}{\partial x_j} + \frac{1}{Sc}\frac{\partial}{\partial x_j}\left(\mu\frac{\partial f}{\partial x_j}\right) \quad , \quad (40)$$

where f is the passive scalar and the Schmidt number Sc was fixed at 0.71. For cases with multiple vibrational equations,

the conserved-variable vector takes the form

$$q = \begin{bmatrix} \rho_s \\ \rho u_i \\ \rho E \\ \rho_m e_{v_m} \\ \rho f \end{bmatrix} \quad . \tag{41}$$

The initial condition was designed to trigger the shear layer instability, using

$$u = u_\infty \tanh(2y/\delta^0_\omega) \quad , \tag{42}$$

$$v_{2d} = A\, u_\infty \cos(2\pi x/L_x)\, e^{-y/(10\delta^0_\omega)} \quad , \tag{43}$$

$$v_{3d} = A\, u_\infty \cos(2\pi x/L_x) \cos(2\pi z/L_z)\, e^{-y/(10\delta^0_\omega)} \quad , \tag{44}$$

$$w = 0.0 \quad , \tag{45}$$

where u_∞ is the free-stream velocity, δ^0_ω is the initial vorticity thickness, L_x and L_z are the domain lengths in the streamwise (x) and spanwise (z) directions, and y is the cross-stream coordinate. The y-grid was hyperbolically stretched according to

$$y = 0.5 L_y \frac{\sinh\left(f_{stch}\frac{j-(n_y-1)/2}{(n_y-1)/2}\right)}{\sinh(f_{stch})} \quad , \tag{46}$$

where L_y is the cross-stream domain length, f_{stch} is the stretching factor, j is the grid index in the y-direction, and n_y is the total number of y-points. A stretching factor of 3.0 was used in 2D simulations and 2.2 in 3D simulations. In 2D cases, the v_{2d} excitation with amplitude $A = 0.01$ initiated Kelvin–Helmholtz roll-up, whereas in 3D cases, the v_{3d} excitation with amplitude $A = 0.05$ triggered oblique-mode breakdown, consistent with Ref. 73.

Table III summarises the computational domains. The streamwise domain length $L_x = 2\pi/\alpha$ was chosen using a wavenumber $\alpha\delta^0_\omega = 0.42$, sufficiently large to accommodate both K–H roll-up (2D) and oblique breakdown (3D). Periodic boundary conditions were applied in homogeneous directions, while first-order extrapolation was used at the top and bottom boundaries. The cross-stream domain length L_y was large enough to capture the expected growth of the mixing layer, with an additional sponge zone of 30 grid points to suppress acoustic reflections. The sponge zone applied a binomial filter with strength f_{str}:

$$U = (1 - f_{str})U + f_{str}U_f \quad , \tag{47}$$

where the averaged filtered solution is given by

$$U_f = (U_{fx} + U_{fy} + U_{fz})/3 \quad , \tag{48}$$

with $U_{fx,fy,fz}$ denoting explicit filters of order n, and stencil coefficients obtained from the expansion of $(a-b)^n/2^n$. Filter strengths of $f_{str} = 0.2$ (2D) and 0.25 (3D) were applied, with $n = 2$ in all cases.

Simulations were carried out on the IRIDIS high-performance computing facility at the University of Southampton, using NVIDIA V100 GPUs for two-dimensional cases and NVIDIA A100 GPUs for three-dimensional cases. Table III also lists the simulation efficiency as an indication of computational cost while using a single GPU.

TABLE III: Computational domain and resources.

	2D	3D
N_x	180	270
N_y	325	451
N_z	-	270
L_x	$2\pi\delta^\circ_\omega/\alpha$	
L_y	$1000/15 \times \delta^\circ_\omega$	
L_z	$2\pi\delta^\circ_\omega/\alpha$	
Stretch Factor	3.0	2.0
GPU (NVIDIA)	$V100$	$A100$
Computing Time (s/Iter)	0.025	1.35

TABLE IV: Grid sensitivity study.

Factor	1.0	1.5	2.25	3.375
N_x & N_z	120	180	270	405
N_y	201	301	451	675
dt	2.7e-7	1.8e-7	1.2e-7	8.0e-8

B. Grid sensitivity and a note on symmetry breaking

To assess grid convergence, a sensitivity study was performed by increasing the number of grid points by a factor of 1.5 in all directions. The most challenging case—the three-dimensional thermo-chemical non-equilibrium flow labelled "LT" in Table V—was selected for this evaluation. To isolate grid effects, the Courant–Friedrichs–Lewy (CFL) number was held constant across all simulations. Table IV summarises the refinement factors, grid densities, and time steps used. The grid dimensions were adjusted to be even for the x and z-direction and odd for the y-direction in order to be able to evaluate the centre of roll up, stagnation point and the centreline. Domain specifications and computational details are given in Table III.

Figure 2 presents the integral turbulent kinetic energy (ITKE) and momentum thickness—two global parameters characteristic of the setup—evaluated at several times during the shear-layer development. Grid densities were compared at identical physical times for each data point. During the vortex development phase, convergence is achieved for refinement factors above 1.5. The later development shows a divergence between cases, and the reasons for this are investigated next by considering a breakdown of a symmetry in the flow.

The mixing layer is initiated with a spanwise symmetry about $z = L_z/2$, which is preserved through the linear growth phase and into the early stages of transition. Figure 3 shows the absolute difference in density and pressure across the symmetry plane, illustrating how symmetry gradually breaks down. The process occurs in three stages. First, during the initial 0–100 iterations, asymmetry arises primarily near the outer boundaries where filtering is applied. Application of the filter introduces small numerical errors that seed the asymmetry. Second, between 100 and 450 iterations, the vortex formation remains essentially symmetric, indicating that early dynamics are insensitive to these small errors.

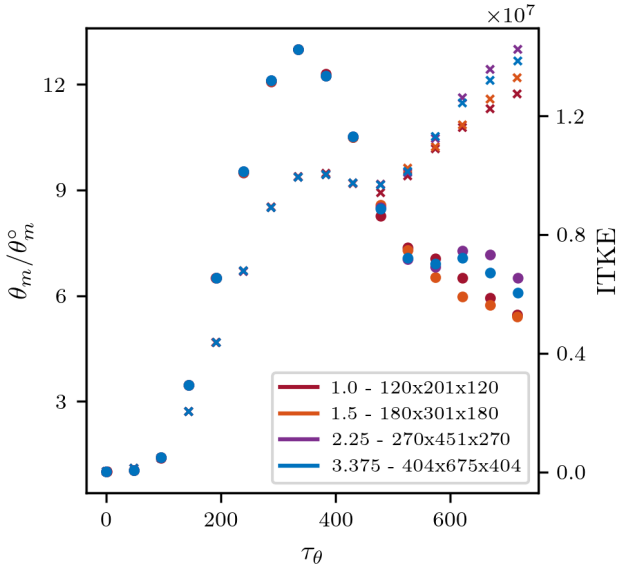

FIG. 2: Grid sensitivity study showing the integral turbulent kinetic energy (ITKE) and momentum thickness. Cross (×) markers indicate momentum thickness; circles (○) indicate ITKE. Colours denote grid resolution.

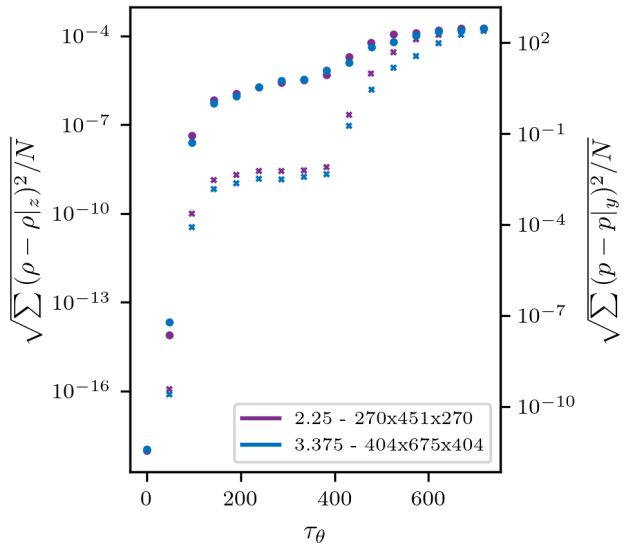

FIG. 3: Flow symmetry of density and pressure across the z and y axis respectively. Density is shown by cross (×) markers and pressure by circles (○).

Third, from 450 to 700 iterations—after the initial peak in momentum thickness—the vortices undergo breakdown to turbulence, and inherent asymmetry emerges as coherent structures cascade into smaller scales. This staged loss of symmetry explains the divergence in the grid sensitivity study: as the flow transitions from deterministic to non-deterministic behaviour, the instantaneous turbulent field becomes sensitive to small perturbations, including grid resolution (and, as will be discussed later, thermo-chemical modelling assumptions).

C. Statistical Quantities

Favre (mass-weighted) averaged quantities are defined as[69]

$$\omega = \tilde{\omega} + \omega'' \quad , \qquad \text{and} \qquad \overline{\omega''} \neq 0 \quad , \tag{49}$$

where $\tilde{\omega}$ is the density-weighted average defined by $\overline{\rho\omega}/\bar{\rho}$, and averaging is carried out in the homogeneous x and z directions. Turbulence normal stresses are defined as

$$\bar{\rho}\widetilde{u''u''}/(\rho_\infty \Delta U^2) \quad , \quad \bar{\rho}\widetilde{v''v''}/(\rho_\infty \Delta U^2) \quad , \quad \bar{\rho}\widetilde{w''w''}/(\rho_\infty \Delta U^2) \quad , \tag{50}$$

and the shear stress as[16]

$$\bar{\rho}\widetilde{u''v''}/(\rho_\infty \Delta U^2) \quad . \tag{51}$$

where ρ_∞ is the freestream density and ΔU is the velocity difference between the two streams. Additionally, quantities related to thermal non-equilibrium are defined as

$$\bar{\rho}\widetilde{u''e_v''}/(\rho_\infty e_{v_\infty}\Delta U), \quad \bar{\rho}\widetilde{v''e_v''}/(\rho_\infty e_{v_\infty}\Delta U), \quad \bar{\rho}\widetilde{w''e_v''}/(\rho_\infty e_{v_\infty}\Delta U). \tag{52}$$

A budget of y-integrated turbulence stresses is defined by[13]

$$\frac{d}{dt}\int \overline{\rho u_i'' u_j''} dy \;=\; P_{ij} + \Pi_{ij} - \varepsilon_{ij}, \tag{53}$$

where

$$P_{ij} = -\int \left(\overline{\rho u_i'' v''}\frac{\partial \tilde{u}_j}{\partial y} + \overline{\rho u_j'' v''}\frac{\partial \tilde{u}_i}{\partial y} \right) dy \,, \tag{54}$$

$$\Pi_{ij} = \int \overline{p\left(\frac{\partial u_i''}{\partial x_j} + \frac{\partial u_j''}{\partial x_i} \right)} dy \,, \tag{55}$$

$$\varepsilon_{ij} = \int \left(\overline{\sigma_{ik}\frac{\partial u_j''}{\partial x_k}} + \overline{\sigma_{jk}\frac{\partial u_i''}{\partial x_k}} \right) dy \,, \tag{56}$$

which refer to the integrated production, pressure strain and dissipation tensors, respectively.

The development of turbulence with time is monitored with an integral of turbulence kinetic energy (ITKE) per unit mass, defined by

$$ITKE = \frac{1}{2}\int_{-\infty}^{\infty} (\widetilde{u''u''} + \widetilde{v''v''} + \widetilde{w''w''}) dy \quad . \tag{57}$$

The momentum thickness of a temporally developing mixing layer is defined as[12]

$$\theta(t) = \frac{1}{\rho_\infty (\Delta U)^2}\int \overline{\rho}(u_1 - \tilde{u})(\tilde{u} - u_2)\, dy \quad , \tag{58}$$

where subscripts 1 and 2 refer to the upper and lower streams, respectively. A reference length is the initial momentum thickness $\theta_\circ$ and a dimensionless time τ_θ is given by[12]

$$\tau_\theta = \frac{t\Delta U}{\theta_\circ} \quad . \tag{59}$$

The momentum thickness growth rate is important, as it has been shown to be proportional to the integrated turbulence production in the form[13]

$$d\theta/dt = -\frac{2}{\rho_\infty(\Delta U)^2}\int\left(\overline{\rho u_1'' u_2''}\frac{\partial \tilde{u}}{\partial y}\right)dy \quad . \tag{60}$$

A vibrational Damköhler number is used to evaluate the correlation between the flow and vibrational timescales, defined as

$$Da_m = \frac{\tau_{flow}}{\tau_m} \quad , \qquad Da_v = \frac{\tau_{flow}}{\tau} \quad . \tag{61}$$

where τ_m is the vibrational relaxation time for molecule m,τ_{flow} is the flow timescale defined as $\theta_\circ/\Delta U$, and τ is the single vibrational relaxation time defined as Eq. 34. If the vibrational Damköhler number is small, the flow can be assumed to be thermally frozen, while large values indicate that the flow is in thermal equilibrium. To compare equilibrium and non-equilibrium cases, the percentage difference of a quantity ϕ is defined as

$$\Delta\phi = \frac{(\phi_{TCNE} - \phi_{EQ}) \times 100}{\phi_{EQ}} \quad . \tag{62}$$

V. SIMULATIONS

Direct numerical simulations are performed using the kinetic models and flow setup described earlier, for two distinct conditions. The first corresponds to a temperature of 3000 K, where the fluid consists of a mixture of air atoms and molecules. The second case considers a higher temperature of 6000 K while maintaining the same flow density. This scenario represents a condition in which vibrational energy is carried primarily by a single molecular species (N_2). Both flow conditions are modelled as thermally and chemically reacting flows, initialised with thermal and chemical equilibrium. Table V summarises the initial conditions for the two cases, denoted as low temperature (LT, with $T_\infty = 3000$ K) and high temperature (HT, with $T_\infty = 6000$ K). The freestream compositions are specified as [0.053, 0.137, 0.000, 0.772, 0.038] and [0.208, 0.000, 0.227, 0.562, 0.003] for the species mass fractions $[Y_O, Y_{O_2}, Y_N, Y_{N_2}, Y_{NO}]$ in the LT and HT cases, respectively. In all simulations, the diffusion model defined by Eq. 14 is used.

In thermally non-equilibrium flows, the relaxation time governing energy exchange between translational and vibrational modes is the dominant factor determining the thermal state of the gas. A longer relaxation time delays equilibration, whereas a shorter relaxation time promotes a faster return to equilibrium. For the flow conditions considered here, the flow timescale is found to be small or comparable to the vibrational relaxation timescales. Consequently, regions of the flow remain out of equilibrium between translational and vibrational modes. In contrast, the chemical timescales are significantly shorter than the flow timescale, resulting in a near-equilibrium chemical state throughout the development of the mixing layer. Table VI defines the acronyms used to refer to the modelling of the simulations carried out.

A. Two Dimensional Mixing Layer

For each of the specified flow conditions in Table V, two simulations were conducted: one under thermal equilibrium and the other under thermal non-equilibrium, with both simulations incorporating chemical reactions. Figure 4 illustrates the two-dimensional mixing layer for the high-temperature (HT) flow condition. Each square depicts the same region of the domain, with each row representing different flow properties and each column corresponding to a distinct time of the simulation, shown as the non-dimensional time on the first row. Row (a) displays the passive scalar, a quantity ranging between 1 (upper stream) and -1 (lower stream). The passive scalar serves as an effective tool for observing the progression of the vortex roll-up. Rows (b), (c), and (d) show the pressure, translational temperature, and vibrational temperature, respectively. The min/max limits of the figure are set to be approximately symmetric about the freestream conditions, allowing the coloured regions to show deviations from the initial conditions. As the vortex develops, a reduction in pressure and temperature is observed at the vortex core, accompanied by an increase in temperature at the stagnation point.

As sketched in Fig. 1, regions of expansion and compression emerge within the flow field that can affect the thermal response. Row (e) of Fig. 4 presents the difference between vibrational and translational temperatures, $T_v - T$, indicating the degree of thermal non-equilibrium. As the vortex develops, the core experiences a drop in translational temperature, while the stagnation point exhibits an increase. Due to the finite energy exchange timescales between translational and vibrational modes, a lag occurs in the vibrational temperature response. This results in regions of hot thermal non-equilibrium, highlighted by red contours, where the vibrational temperature lags behind a reduction in translational temperature, and regions of cold thermal non-equilibrium where it lags behind an increase in translational temperature. Areas of flow expansion (associated with decreasing translational temperature) are associated with a hot thermal non-equilibrium, while areas of compression exhibit a cold thermal non-equilibrium. In this high-temperature case, the vibrational mode is governed solely by nitrogen molecules. Finally, row (f) depicts the extent of chemical non-equilibrium for nitrogen molecules, expressed as a percentage (Eq. 62). As previously noted, chemical non-equilibrium remains minimal throughout the vortex development due to the significantly shorter timescales of chemical reactions. Overall, the effects of free stream temperature and thermal non-equilibrium on the mixing layer evolution are not large. Figure 5 shows the momentum thickness (normalised with its initial value) as a function of the normalised time given by Eq. 59 for the LT and HT cases, each carried out for thermal equilibrium (CNE) and

TABLE V: Initial conditions for the low-temperature (LT) and high-temperature (HT) cases.

Case	$u_\infty\ (m/s)$	$T_\infty\ (K)$	$\rho_\infty\ (kg/m^3)$	$p_\infty\ (N/m^2)$	$dt\ (s)$	$\delta^\circ_\omega\ (m)$	Re_{δ°	M_c	Model
LT	439	3000	0.02	18174	1.4e-7	0.004013943	400	0.4	TCNE
HT	752	6000	0.02	49271	7.0e-8	0.004169621	400	0.4	TCNE

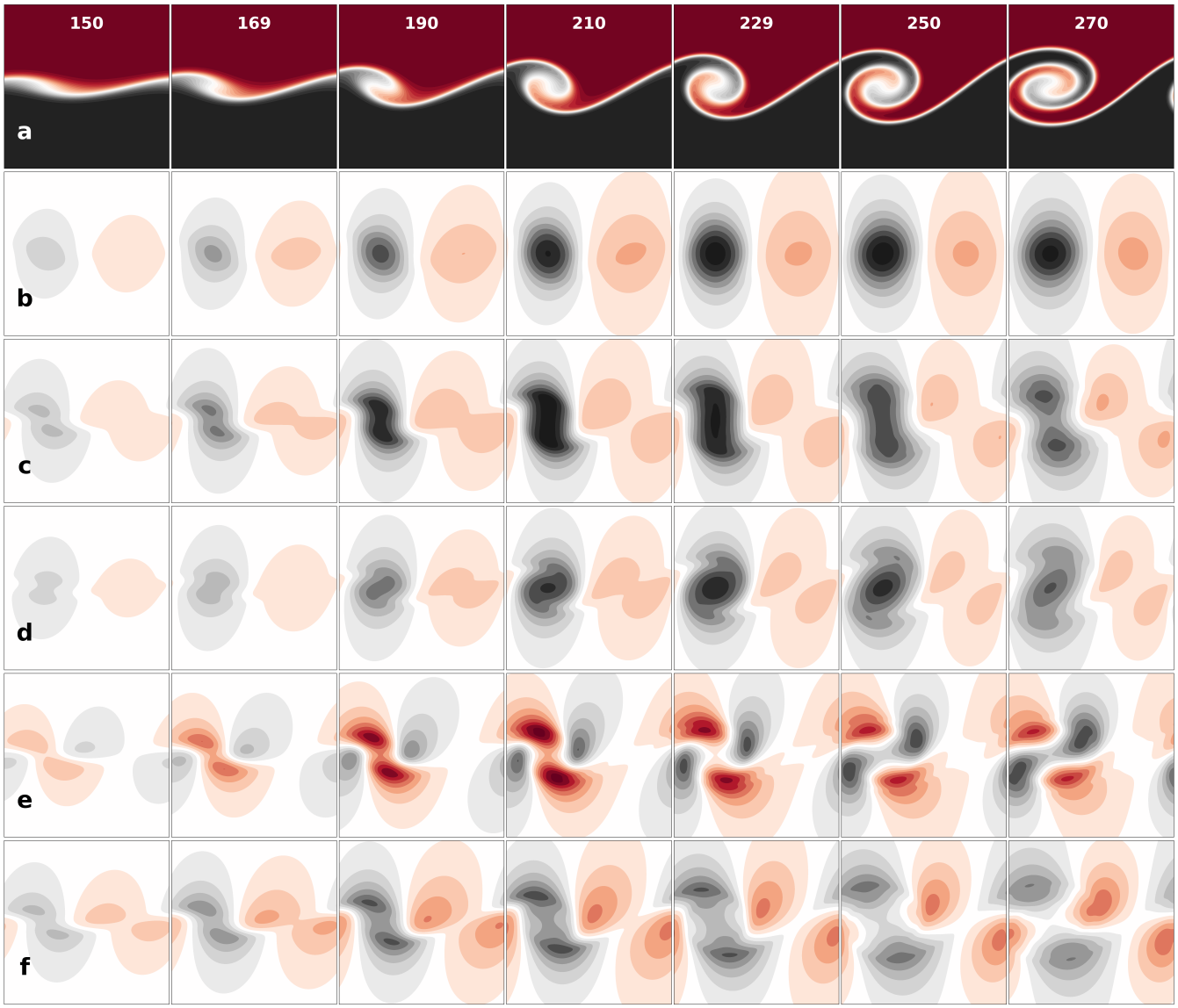

FIG. 4: Two dimensional temporal mixing layer with thermo-chemical non-equilibrium for HT case, with non-dimensional time τ_θ displayed in the first row. a) passive scalar [min:-1, max:+1], b) pressure in Pa [min:36139, max:62139], c) translational temperature in Kelvin [min:5750, max:6250], d) vibrational temperature in Kelvin [min:5750, max:6250], e) thermal non-equilibrium ($T_v - T$) in Kelvin [min:-130, max:130], f) percentage chemical non-equilibrium of Nitrogen molecules (N_2) [min:-0.004, max:0.004].

thermo-chemical non-equilibrium (TCNE) conditions. Both conditions use the multi-e_v formulation as defined in Section II A. The HT case shows a slightly delayed increase in mixing layer thickness due to vortex roll-up. Figure 6 shows the percentage difference in the spatial integral of turbulence kinetic energy (ITKE) between the equilibrium (CNE) and thermal non-equilibrium (TCNE) flow states, as defined by Eq. 62. Thermal non-equilibrium causes an increase in turbulence kinetic energy (TKE) relative to equilibrium state, consistent with the slightly earlier rise in momentum thickness. To highlight the differences between employing a single vibrational energy conservation equation

TABLE VI: Definition of acronyms for thermal and chemical equilibrium states.

Acronym	Thermal	Chemical
TCNE	Non-equilibrium	Non-equilibrium
CNE	Equilibrium	Non-equilibrium
TNECF	Non-equilibrium	Frozen
CF	Equilibrium	Frozen

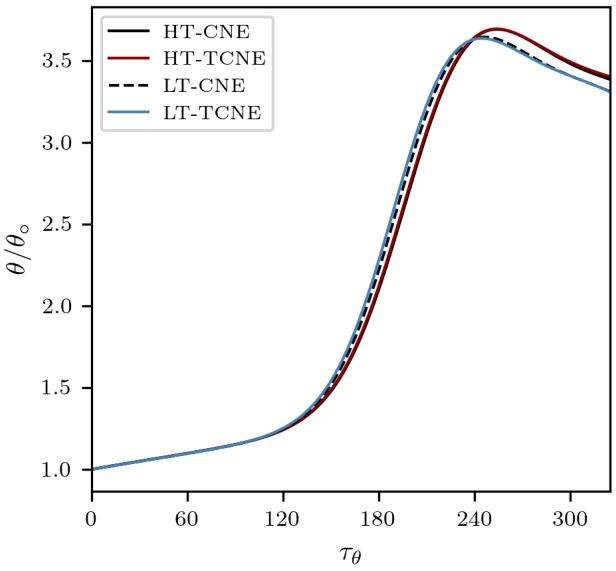

FIG. 5: Normalised momentum thickness against non-dimensional time.

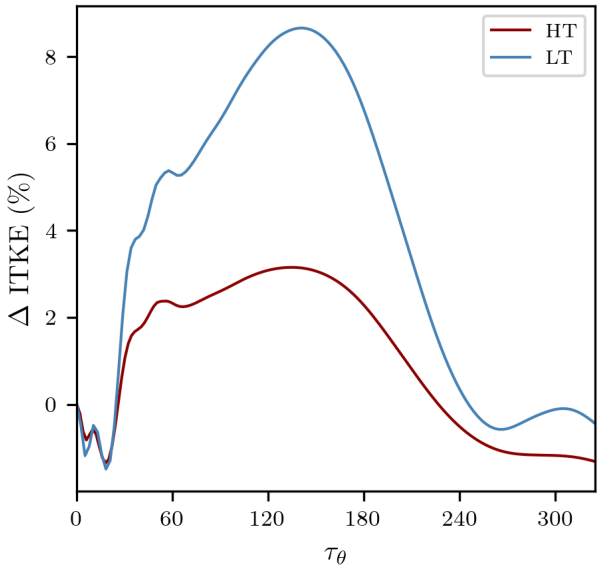

FIG. 6: Difference in ITKE between the thermal equilibrium and non-equilibrium cases for the HT and LT cases.

and a formulation that accounts for the conservation of vibrational energy for each molecular species individually, the low-temperature (LT) flow condition is used, as described in Table V. In this case (in contrast to the HT case) the contribution to the internal energy modes arises from N_2, O_2 and NO molecules. Under these conditions, the impact of averaging relaxation times becomes more pronounced.

Figure 7 illustrates the differences between the two kinetic models (single-e_v vs. multi-e_v) in terms of the temperature difference between the translational and vibrational modes. Row (a) presents the passive scalar, while (b) depicts the extent of thermal non-equilibrium for the single-e_v model, and (c) shows the corresponding non-equilibrium $T_v - T$ for the multi-e_v model. The relaxation timescales of the two models differ significantly. The multi-e_v model results in a more highly concentrated non-equilibrium region at the centre of the roll-up, mimicking a thermally frozen state. This difference in relaxation behaviour arises from how the relaxation time is considered within each model. The multi-e_v model captures the contribution of the slower relaxation associated with N_2, whereas the single-e_v model, due to averaging, skews the relaxation time towards the faster relaxation characteristic of O_2. When considering the higher mass fraction of N_2, this averaging approach leads to an underestimation of nitrogen's contribution to the energy exchange between translational and vibrational modes. It should be noted that the governing equations defined for the multi-e_v model do not account for vibrational-vibrational energy exchange. Therefore, the differences observed reflect a scenario in which inter-species relaxation is considerably slower relative to translational-vibrational modes. In this scenario, the discrepancies are significant. In terms of computational cost, the single-e_v model was found to provide savings of less than $\sim 3\%$ in run time compared to the multi-e_v model, so the only drawback of the multi-e_v model is the increased storage associated with having a transport equation for each molecular species. In the present cases this increases the number of equations (including the passive scalar) from 11 to 13.

The two flow conditions examined (LT and HT, comparing Figs. 4 and 7) demonstrate distinct qualitative characteristics of thermal non-equilibrium within the flow field. In one case (Fig. 4e), a mixture of cold and hot non-equilibrium regions forms a quadrupole-like pattern around the vortex, where the thermal state responds to flow kinetics by reacting to compression and expansion, respectively. In contrast, Fig. 7c shows that the thermal energy exchange is too slow to respond effectively to regions of compression and expansion within the flow field, resulting in a thermally hot vortex core, i.e. the free-stream flow is fully entrained before it is able to relax to match the translational temperature. Across the simulated cases, three primary regions can be identified where the flow departs from equilibrium: the entrainment region, the vortex core, and the stagnation point. When the relaxation time is shorter, these regions tend towards equilibrium. Conversely, when the relaxation time is sufficiently long to induce a thermally frozen state, these regions remain in a non-equilibrium condition throughout the flow evolution.

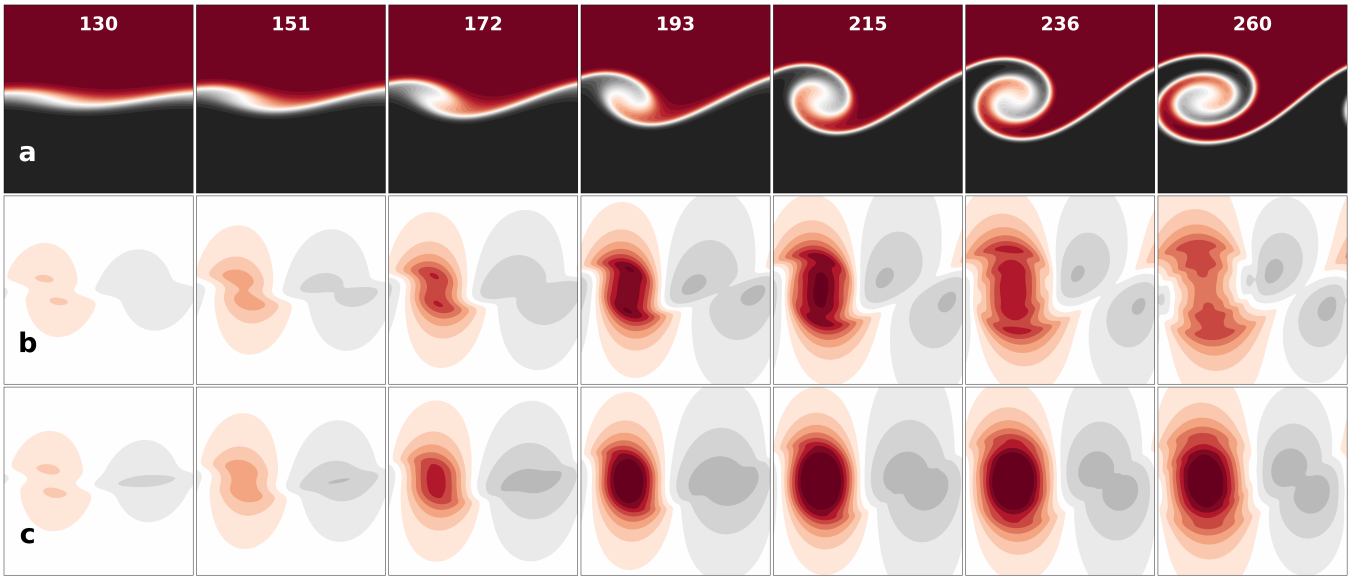

FIG. 7: Mixing layer simulation for the lower temperature (3000K) case comparing the single to multi vibrational energy conservation equation. a) passive scalar [min:-1, max:+1], b) $T_v - T$ for single-e_v model in Kelvin [min:-130, max:130], c) $T_v - T$ for multi-e_v model in Kelvin [min:-130, max:130].

Vibrational Damköhler numbers based on the initial mixing layer momentum thickness (see Eq. 61) are shown in Table VII. The choice of timescale affects the absolute values. For example, if we use a characteristic roll-up time of the vortex, from the start of non-linear growth of disturbances up to non-linear saturation (see Figs. 4 and 5), the numbers would be two orders of magnitude higher. For the most important molecular contributor, Da_{N_2} is a factor of 30 higher for the HT case. It can also be seen that the mixture Da is also much higher for the HT case. These relative values are consistent with the HT case being in non-equilibrium and the LT case (with the $3e_v$ model) being closer to frozen.

While the qualitative description of thermal non-equilibrium for the LT case (Fig. 7) with the single-e_v model is closer to that described earlier for the high-temperature case (Fig. 4e), the development is distinct. Following the initial departure from equilibrium at the core and stagnation point, the non-equilibrium state persists and intensifies as the vortex continues to roll up. This leads to a higher region of hot non-equilibrium within the vortex core, alongside a cold non-equilibrium state in the stagnation region. This is consistent with the previous comments that the use of a single vibrational energy conservation equation in this case results in a faster overall relaxation timescale, leading to an underestimation of the influence of thermal non-equilibrium.

TABLE VII: Vibrational Damköhler numbers for molecules and for the mixture

	Da_{O_2}	Da_{N_2}	Da_{NO}	Da_v
LT	0.1169	0.0028	0.0238	0.0187
HT	1.0931	0.0909	0.3811	0.0909

B. Three Dimensional Mixing Layer

Three-dimensional (3D) simulations were conducted for the same flow conditions specified in Table V to evaluate whether the conclusions drawn in the previous section with respect to thermal non-equilibrium can be carried over to the fully 3D cases. These cases were carried out using the multi-e_v formulation with initial conditions similar to those defined earlier. Figure 8 illustrates the flow development within a three-dimensional domain, where the top row is the LT case, the bottom row is the HT case and each column corresponds to a different time during the vortex roll-up (times of $\tau_\theta = 200$, 300, and 500). Iso-surfaces of the Q-criterion at 1.0×10^{10} and 2.0×10^{10} respectively are shown, overlaid with colour contours of $T_v - T$, indicating the extent of thermal non-equilibrium (in K).

Following the introduction of the initial disturbance, oblique-mode instabilities give rise to the formation of vortical tubes within the shear layer. These inclined vortex tubes deform[74] into hairpin-like vortices, with the same structure on the lower side due to a cross-stream symmetry of the initial disturbance. The evolution of the vortices is accompanied by regions of thermal non-equilibrium. Similarly to the two-dimensional cases, the slower thermal relaxation in the LT case results in persistent regions of hot thermal non-equilibrium throughout the vortex roll-up, extending from the core to the point of breakdown. In contrast, the faster relaxation in the high-temperature case produces a combination of cold and hot thermal non-equilibrium around the vortical tubes. As the hairpin head

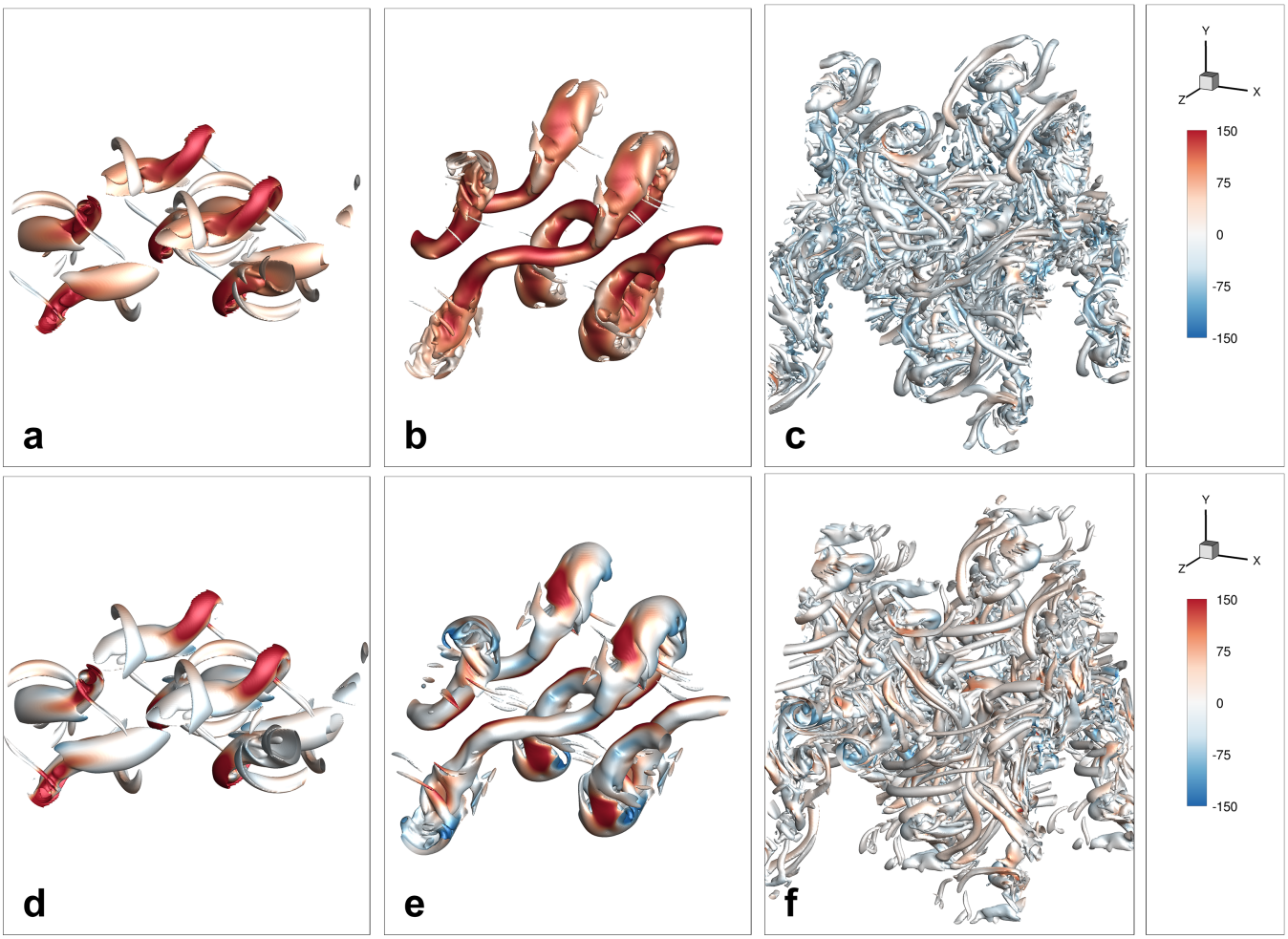

FIG. 8: Iso-surface of Q-Criterion for three dimensional temporally developing mixing layer coloured by $T_v - T$. (a)-(c) correspond to LT case and (d)-(f) to HT during the flow development with τ_θ of 200, 300 and 500.

develops, flow is accelerated and the translational temperature reduces, generating a hot thermal non-equilibrium region, while compression on the lower side leads to the formation of a cold non-equilibrium, shown in blue on Fig. 8(e).

These observations extend the findings from the two-dimensional simulations, indicating that the formation of non-equilibrium flow regions is highly dependent on local compression and expansion of the flow, while the persistence of non-equilibrium regions within the flow field depends on the thermal relaxation time. This characteristic is similar to that seen by Ref. 9 where the vibrational non-equilibrium was seen to be caused by compressibility effects, although the authors also showed thermal relaxation does not always follow the Landau-Teller model. Similar observations where thermal non-equilibrium is sustained by turbulence have been made in other flows[4,5,7]. According to the Kolmogorov cascade, one can speculate that the small-scale motions would have shorter time scales and become more thermally frozen, but this is not seen in the present low Reynolds number simulations. Instead, following the development of the hairpin vortex head, the vortices break down and small-scale structures continue to exhibit varying non-equilibrium states, maintaining the qualitative characteristics identified earlier.

Figure 9 shows the evolution of momentum thickness for the three-dimensional cases, with vertical bars used to identify averaging zones to be discussed later. As observed in previous studies[12,13,75], the momentum thickness exhibits an initial region with a high growth rate. The peak in momentum thickness at $\tau_{\theta_0} \approx 350$ is associated with the non-linear saturation of the hairpin vortex. Subsequently, the momentum thickness starts to grow again, driven only by small-scale structures, since the shear layer has grown and the relative size of the computational box is no longer large enough to sustain oblique-mode instabilities at large scale. The influence of thermal non-equilibrium in the early stages of hairpin vortex development is small.

The divergence in the curves at later times is partly due to the amplification of small differences in initial conditions, resulting in different trajectories in the phase space of the non-linear system. That the present system behaves in this way was demonstrated by the symmetry breaking shown in Fig. 3. In addition, the LT case is sensitive to the chemistry

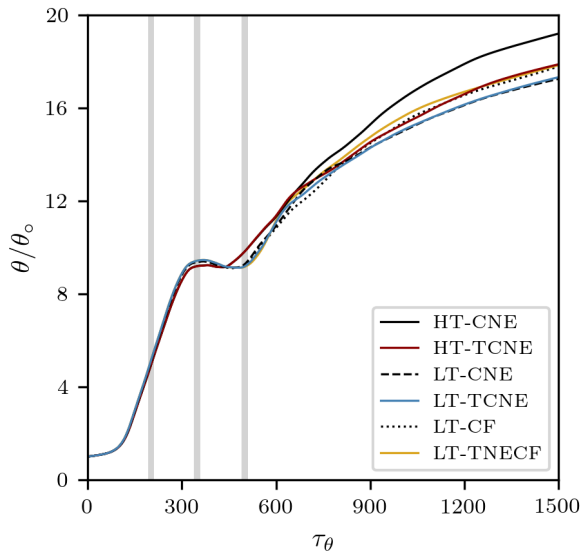

FIG. 9: Non-dimensional momentum thickness for the 3D simulations.

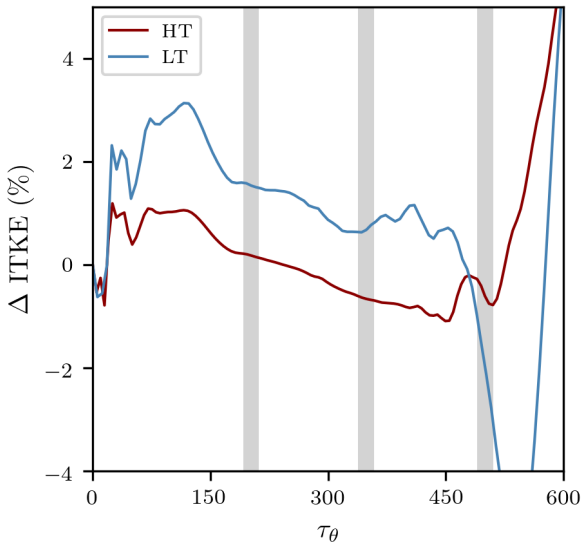

FIG. 10: Integral of turbulence kinetic energy compared with the three dimensional equilibrium case, shown in percentage.

(frozen vs non-equilibrium) and the chemistry is sensitive to the thermal state (equilibrium or non-equilibrium). Improved averages could be generated by ensemble averaging over multiple simulations with slightly different initial conditions, or by running large-domain simulations with randomised initial conditions, but this is not attempted here.

Figure 10 presents the percentage difference in the integrated turbulence kinetic energy (ITKE) between the equilibrium and non-equilibrium simulations. As in the two-dimensional cases, ITKE increases during the development of the mixing layer, although the magnitude of the differences is smaller. At later times ($\tau_\theta > 500$), larger variations appear. Similar to the momentum thickness, these are attributed to the non-linear amplification of smaller differences from the earlier evolution.

Turbulence statistics are shown in Fig. 11. To obtain smoother profiles, averaging was applied using six flow fields within three time intervals, centred at $\tau_\theta = 200, 350, 500$, corresponding to the shaded regions in Figs. 9 and 10. Figures 11a to 11d present the non-dimensional Reynolds stresses corresponding to the normal and shear stresses arising from momentum transfer by the fluctuating velocity field. The normal stresses show an increase in fluctuations in the central region of the shear layer, associated with the formation of vortex tubes. With the development of the hairpin vortex heads, a splitting of the peak in the term $\bar{\rho}\widetilde{u''u''}/(\rho_\infty \Delta u_\infty^2)$ occurs. In contrast, a significant increase along the centreline is observed as a single peak in the term $\bar{\rho}\widetilde{v''v''}/(\rho_\infty \Delta u_\infty^2)$ in Fig. 11b, while the term $\bar{\rho}\widetilde{w''w''}/(\rho_\infty \Delta u_\infty^2)$, shown in Fig. 11c, shows a transient reduction in lateral fluctuations.

The shear stress (Fig. 11d) spreads progressively in the y-direction and decreases as the shear layer grows. The influence of thermal non-equilibrium on Reynolds stresses is minimal during the vortex development and initial peak in momentum thickness (up to $\tau_\theta = 350$). While the effects are small in the present case, experimental studies in channel flows with plasma heating[76] have reported reductions of up to 50% in Reynolds stress. In cases where higher vibrational modes are excited, improved relaxation models[9] are likely to be needed. Turbulence introduces additional flux terms in the vibrational energy equation. Figures 11e and 11f show two such fluxes, where clear differences emerge between equilibrium and non-equilibrium cases. The peaks of the term $\bar{\rho}\widetilde{u''e_v}$ are slightly below the locations of the heads of the hairpin vortex tubes (see Fig. 8b). For example, at $\tau_\theta = 350$ in Fig. 11e, the locations $y/\theta_\circ = \pm 22$ correspond to the cores of the hairpin vortices, whereas the peak is at $y/\theta_\circ \approx \pm 17$. In contrast, for the term $\bar{\rho}\widetilde{v''e_v}$ shown in Fig. 11f, the peak values occur much closer to the centreline. In both cases, thermal non-equilibrium reduces vibrational fluctuations. This reduction may be interpreted as a dampening of peak fluctuations due to the weaker coupling of the vibrational mode compared to the translational mode, such that the vibrational temperature does not fully inherit the variability present in the translational temperature field.

Figure 11g presents the translational temperature fluctuations, $\widetilde{T''T''}/T_\infty^2$, which increase in the presence of thermal non-equilibrium. In the present mixing layer configuration, the vortex core is characterised by reduced translational temperature, which is amplified under non-equilibrium conditions. The resulting stronger gradients in translational temperature play a role in enhancing transport by fluctuating terms.

Thermal non-equilibrium within the flow field has previously been attributed to translational temperature fluctuations[2,4,8,9]. This is confirmed when comparing Figs. 11g and 11h, where the profiles of the averaged non-equilibrium correlate with those of temperature

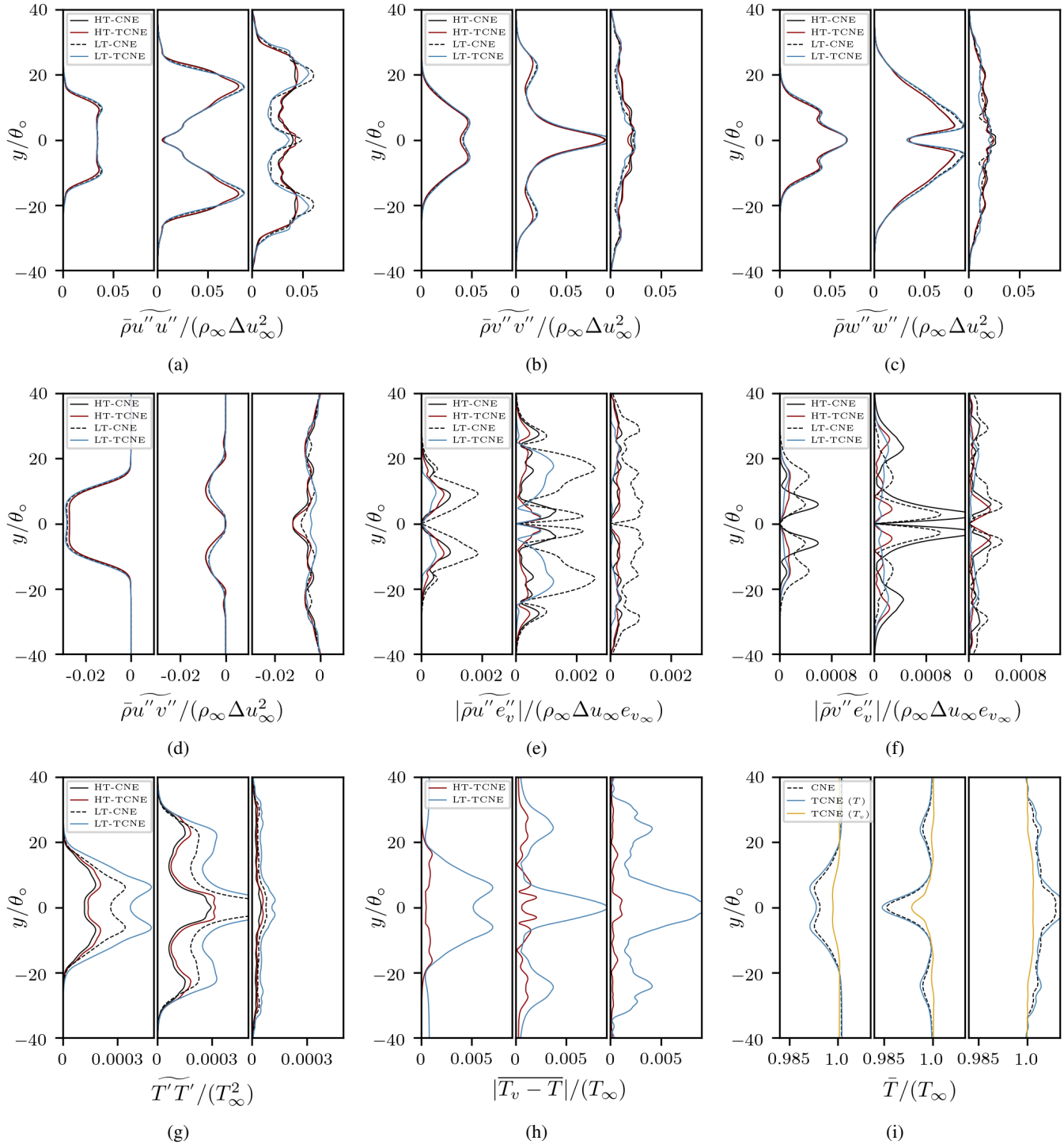

FIG. 11: Statistical analysis of the mixing layer across the shear layer for non-dimensional times of $\tau_\theta = 200, 350$ and 500.

fluctuations. In Fig. 11h, the higher-temperature case exhibits a steeper gradients across the shear layer, which may be associated with the coexistence of hot and cold non-equilibrium regions that partially offset each other when averaged.

Figure 11i displays the mean translational and vibrational temperatures across the shear layer for the lower-temperature case. As expected, the mean translational temperature is initially reduced across the layer, reflecting the cooling in vortex cores. A comparison between equilibrium and non-equilibrium cases reveals an additional reduction in the translational mean temperature for non-equilibrium and a corresponding increase in the vibrational mean temperature (in CNE, $T_v = T$). This behaviour is attributed to the slower

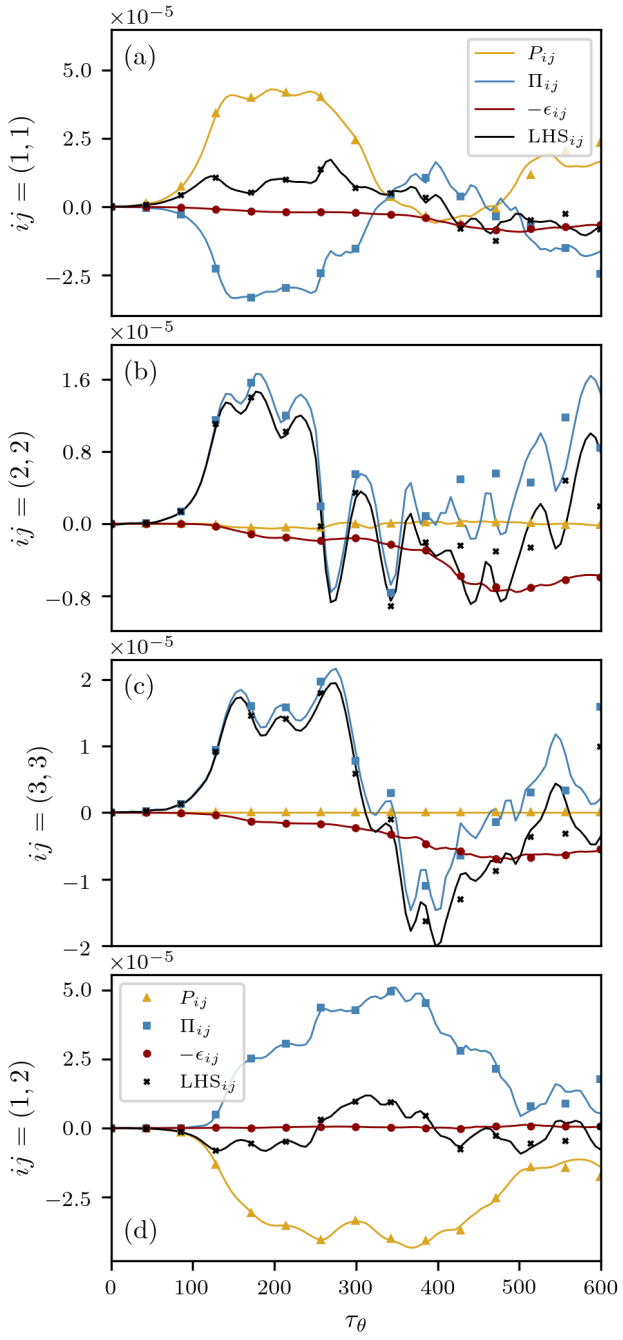

FIG. 12: Energy budget of the lower temperature case. Solid lines refer to the CNE case where markers are for the TCNE case. P_{ij} is the integral of production, Π_{ij} is the pressure-strain, $-\epsilon_{ij}$ is the dissipation and LHS is the integrated Reynolds stress defined as $\frac{d}{dt}\int \overline{\rho u_i'' u_j''} dy$.

vibrational relaxation in the LT case, which prolongs the energy exchange between the translational and vibrational modes. As a result, the vibrational mode retains a larger fraction of the total energy, further lowering the translational temperature compared with its equilibrium counterpart. Reductions of the mean translational temperature have been

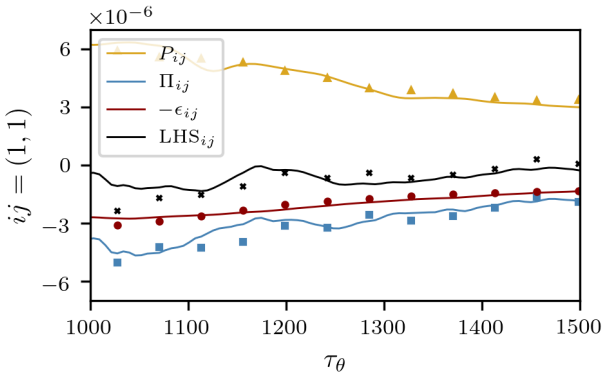

FIG. 13: Energy budget of the component $(1,1)$ in the later stages of the simulation

reported in other studies of compressible shear layers[8], however in that case the central region of the mixing layer was hot relative to the freestream, whereas in the present case it is cool. Therefore, in the present case the temperature difference between the centre and freestream is increased, whereas in Ref. 8 it is reduced. In each case the temperature fluctuations scale with magnitude of the difference in temperature between the mixing layer centre and the freeestream. Both cases are possible in practice. For example, in a laboratory experiment, a mixing layer could develop behind a splitter plate under hot or cold wall conditions.

Figure 12 shows the time variation of terms in energy budget for the LT case. Each sub-figure corresponds to a different stress component; the $(1,3)$ and $(2,3)$ components are omitted as they are negligible for this configuration. Colours denote the contributions of different terms to the integrated Reynolds stresses, while markers indicate the corresponding quantities for the TCNE case. During the initial growth of momentum thickness ($\tau_\theta = 150$–300), both the growth rate and production remain nearly constant, consistent with Eq. 60. The pressure–strain term is negative for the $(1,1)$ component and positive for the $(2,2)$ and $(3,3)$ components, indicating redistribution of energy from streamwise fluctuations into the normal and spanwise fluctuations[13]. With the emergence of small-scale turbulent structures, the link between growth rate and integrated production breaks down. This transition, evident for $\tau_\theta > 300$, also highlights differences between the CNE and TCNE cases, consistent with the nonlinear dynamics discussed earlier. In the early stages of flow development and breakdown, differences between the CNE and TCNE cases are minor, similar to those observed in ITKE (Fig. 10). In the later stages ($\tau_\theta = 1200$–1500), dissipation becomes comparable to production and pressure–strain. Figure 13 shows the budget for the $(1,1)$ component, illustrating that dissipation contributes substantially to the Reynolds stress budget at later times.

VI. CONCLUSION

This study has evaluated the extent to which thermo-chemical non-equilibrium influences the breakdown to turbulence in a temporally-developing mixing layer, while also assessing the implications of common modelling approximations. Two flow conditions at low and high temperatures (LT and HT) were considered to cover a range of Damköhler numbers. Two-dimensional simulations revealed two distinct patterns of thermal non-equilibrium formation. In the HT case, thermal and flow timescales were comparable, leading to alternating hot and cold non-equilibrium regions around the vortex entrainment. In the LT case, thermal relaxation was significantly slower than the flow timescale, resulting in persistent thermal non-equilibrium within the vortex core, effectively representing a thermally frozen state. For both cases, only minor differences in momentum thickness were observed between equilibrium and non-equilibrium simulations. However, turbulence kinetic energy (TKE) increased by approximately 8% in the LT case and 4% in the HT case, suggesting that thermal non-equilibrium enhances the generation of TKE.

A comparison was made between a model in which vibrational modes of all species were coupled into a single transport equation and a model in which each molecular species had its own vibrational transport equation. Significant differences were identified between the two approaches. In the single-equation model, averaging led to an underestimation of relaxation times, as relaxation shifted towards the faster O_2 rates rather than the slower N_2 rates, despite the latter dominating the mixture. In the multi-equation approach, more complete modelling of vibrational–vibrational relaxation is required to fully assess the magnitude of this effect.

The three-dimensional simulations revealed similar qualitative patterns of thermal non-equilibrium compared to the two-dimensional cases. In the LT case, large regions of hot non-equilibrium were sustained within vortical cores, whereas in the HT case, a combination of hot and cold regions was observed around individual structures corresponding to the expansion and compression of the flow. Minimal differences in mean and Reynolds stress profiles were observed during the initial stages of vortex development. Turbulence kinetic energy (TKE) increased by approximately 3% in the LT case and 1% in the HT case, suggesting that thermal non-equilibrium marginally enhances the generation of TKE. Differences in later stages were attributed in part to nonlinear dynamics of the breakdown to turbulence (confirmed through a symmetry-breaking study), which amplifies small difference from earlier in the flow development. The statistical results confirmed relationships between mean temperature, thermal non-equilibrium and temperature fluctuations, consistent with prior studies. Energy budgets showed minor differences due to non-equilibrium during the initial growth and breakdown stages.

The present investigation has highlighted significant effects of applying different modelling strategies to intermolecular vibrational energy exchange. More work is needed to develop better physical models of these processes. While the present results indicate a limited influence of thermo-chemical non-equilibrium on hypersonic turbulence, this outcome is specific to the temperature range and species composition considered in this study. In particular, if chemical timescales are comparable to flow timescales, larger effects would be expected. Future research could therefore focus on such regimes, as well as on cases with different temperature ratios across the mixing layer.

ACKNOWLEDGMENTS

The authors acknowledge the use of the Iridis High Performance Computing Facility, and associated support services at the University of Southampton, in the completion of this work.

Appendix A: Transport Properties

Table VIII includes the coefficients defined for the computation of viscosity, total thermal conductivity, ro-translational thermal conductivity and species vibrational thermal conductivity taken from Ref. 41.

Appendix B: Chemical kinetic model

The chemical reactions relating to a five-species air mixture are:

$$
\begin{aligned}
&\text{R1: } \mathrm{N_2 + M \leftrightarrow 2N + M}, && (\mathrm{M = N, O})\\
&\text{R2: } \mathrm{N_2 + M \leftrightarrow 2N + M}, && (\mathrm{M = N_2, O_2, NO})\\
&\text{R3: } \mathrm{O_2 + M \leftrightarrow 2O + M}, && (\mathrm{M = N, O})\\
&\text{R4: } \mathrm{O_2 + M \leftrightarrow 2O + M}, && (\mathrm{M = N_2, O_2, NO})\\
&\text{R5: } \mathrm{NO + M \leftrightarrow N + O + M}, && (\mathrm{M = O, N, NO})\\
&\text{R6: } \mathrm{NO + M \leftrightarrow N + O + M}, && (\mathrm{M = O_2, N_2})\\
&\text{R7: } \mathrm{N_2 + O \leftrightarrow N + NO},\\
&\text{R8: } \mathrm{NO + O \leftrightarrow N + O_2}.
\end{aligned}
$$

Table IX specifies the coefficients for Eq. 29, which defines the forward reaction rate. The equilibrium constant is defined by Eq. 25, and the backward reaction rate is obtained accordingly. The forward reaction rates are:

TABLE VIII: Coefficients for viscosity, translational, and vibrational thermal conductivity models.

	a	b	c	d	e	f	g	h
μ	-2.0989e+05	-5.2310e-06	1.9855e+04	-2.7244e+08	1.2667e+06	3.3933e-04	-1.3007e+05	3.5234e+08
K	3.2315e+02	2.1022e-07	-3.5288e+01	8.0676e+04	-4.5599e+02	-1.8431e-07	4.6392e+01	-3.0308e+05
K_{tr}	2.1762e+02	2.1403e-07	-2.4067e+01	1.0838e+05	-9.8842e+02	-5.1961e-07	1.0492e+02	-2.3396e+05
$K_{v,\mathrm{N_2}}$	1.9200e-04	-3.9290e-06	1.4026e-08	-4.8403e-12	7.5275e-16	-5.0128e-20	1.0884e-24	-
$K_{v,\mathrm{O_2}}$	-1.1446e-03	7.2095e-06	6.2555e-09	-2.6587e-12	4.2901e-16	-2.5152e-20	3.0436e-25	-
$K_{v,\mathrm{NO}}$	-4.2658e-04	9.8630e-07	1.1229e-08	-4.2799e-12	7.0384e-16	-4.8694e-20	1.1027e-24	-

TABLE IX: Coefficients for the chemical kinetic model.

	R_1	R_2	R_3	R_4	R_5	R_6	R_7	R_8
C	3.0×10^{22}	7.0×10^{21}	1.0×10^{22}	2.0×10^{21}	1.1×10^{17}	5.0×10^{15}	5.7×10^{12}	8.4×10^{12}
n	-1.6	-1.6	-1.5	-1.5	0.00	0.00	0.42	0.00
T_f	1.132×10^{5}	1.132×10^{5}	5.936×10^{4}	5.936×10^{4}	7.550×10^{4}	7.550×10^{4}	4.2938×10^{4}	1.940×10^{4}
T_a	$\sqrt{TT_v}$	$\sqrt{TT_v}$	$\sqrt{TT_v}$	$\sqrt{TT_v}$	$\sqrt{TT_v}$	$\sqrt{TT_v}$	T	T

$$R_{f1} = 10^3 k_{f1}\left(\frac{\rho_{\mathrm{N_2}}}{10^3 M_{\mathrm{N_2}}}\right)\left(\frac{\rho_{\mathrm{O}}}{10^3 M_{\mathrm{O}}}+\frac{\rho_{\mathrm{N}}}{10^3 M_{\mathrm{N}}}\right),$$

$$R_{f2} = 10^3 k_{f2}\left(\frac{\rho_{\mathrm{N_2}}}{10^3 M_{\mathrm{N_2}}}\right)\left(\frac{\rho_{\mathrm{O_2}}}{10^3 M_{\mathrm{O_2}}}+\frac{\rho_{\mathrm{N_2}}}{10^3 M_{\mathrm{N_2}}}+\frac{\rho_{\mathrm{NO}}}{10^3 M_{\mathrm{NO}}}\right),$$

$$R_{f3} = 10^3 k_{f3}\left(\frac{\rho_{\mathrm{O_2}}}{10^3 M_{\mathrm{O_2}}}\right)\left(\frac{\rho_{\mathrm{O}}}{10^3 M_{\mathrm{O}}}+\frac{\rho_{\mathrm{N}}}{10^3 M_{\mathrm{N}}}\right),$$

$$R_{f4} = 10^3 k_{f4}\left(\frac{\rho_{\mathrm{O_2}}}{10^3 M_{\mathrm{O_2}}}\right)\left(\frac{\rho_{\mathrm{O_2}}}{10^3 M_{\mathrm{O_2}}}+\frac{\rho_{\mathrm{N_2}}}{10^3 M_{\mathrm{N_2}}}+\frac{\rho_{\mathrm{NO}}}{10^3 M_{\mathrm{NO}}}\right),$$

$$R_{f5} = 10^3 k_{f5}\left(\frac{\rho_{\mathrm{NO}}}{10^3 M_{\mathrm{NO}}}\right)\left(\frac{\rho_{\mathrm{O}}}{10^3 M_{\mathrm{O}}}+\frac{\rho_{\mathrm{N}}}{10^3 M_{\mathrm{N}}}+\frac{\rho_{\mathrm{NO}}}{10^3 M_{\mathrm{NO}}}\right),$$

$$R_{f6} = 10^3 k_{f6}\left(\frac{\rho_{\mathrm{NO}}}{10^3 M_{\mathrm{NO}}}\right)\left(\frac{\rho_{\mathrm{O_2}}}{10^3 M_{\mathrm{O_2}}}+\frac{\rho_{\mathrm{N_2}}}{10^3 M_{\mathrm{N_2}}}\right),$$

$$R_{f7} = 10^3 k_{f7}\left(\frac{\rho_{\mathrm{N_2}}}{10^3 M_{\mathrm{N_2}}}\right)\left(\frac{\rho_{\mathrm{O}}}{10^3 M_{\mathrm{O}}}\right),$$

$$R_{f8} = 10^3 k_{f8}\left(\frac{\rho_{\mathrm{NO}}}{10^3 M_{\mathrm{NO}}}\right)\left(\frac{\rho_{\mathrm{O}}}{10^3 M_{\mathrm{O}}}\right),$$

where M_s is defined in grams. The backward reaction rates are:

$$R_{b1} = 10^3 k_{b1}\left(\frac{\rho_{\mathrm{N}}}{10^3 M_{\mathrm{N}}}\right)^2\left(\frac{\rho_{\mathrm{O}}}{10^3 M_{\mathrm{O}}}+\frac{\rho_{\mathrm{N}}}{10^3 M_{\mathrm{N}}}\right),$$

$$R_{b2} = 10^3 k_{b2}\left(\frac{\rho_{\mathrm{N}}}{10^3 M_{\mathrm{N}}}\right)^2\left(\frac{\rho_{\mathrm{O_2}}}{10^3 M_{\mathrm{O_2}}}+\frac{\rho_{\mathrm{N_2}}}{10^3 M_{\mathrm{N_2}}}+\frac{\rho_{\mathrm{NO}}}{10^3 M_{\mathrm{NO}}}\right),$$

$$R_{b3} = 10^3 k_{b3}\left(\frac{\rho_{\mathrm{O}}}{10^3 M_{\mathrm{O}}}\right)^2\left(\frac{\rho_{\mathrm{O}}}{10^3 M_{\mathrm{O}}}+\frac{\rho_{\mathrm{N}}}{10^3 M_{\mathrm{N}}}\right),$$

$$R_{b4} = 10^3 k_{b4}\left(\frac{\rho_{\mathrm{O}}}{10^3 M_{\mathrm{O}}}\right)^2\left(\frac{\rho_{\mathrm{O_2}}}{10^3 M_{\mathrm{O_2}}}+\frac{\rho_{\mathrm{N_2}}}{10^3 M_{\mathrm{N_2}}}+\frac{\rho_{\mathrm{NO}}}{10^3 M_{\mathrm{NO}}}\right),$$

$$R_{b5} = 10^3 k_{b5}\left(\frac{\rho_{\mathrm{N}}}{10^3 M_{\mathrm{N}}}\right)\left(\frac{\rho_{\mathrm{O}}}{10^3 M_{\mathrm{O}}}\right)\left(\frac{\rho_{\mathrm{O}}}{10^3 M_{\mathrm{O}}}+\frac{\rho_{\mathrm{N}}}{10^3 M_{\mathrm{N}}}+\frac{\rho_{\mathrm{NO}}}{10^3 M_{\mathrm{NO}}}\right),$$

$$R_{b6} = 10^3 k_{b6}\left(\frac{\rho_{\mathrm{N}}}{10^3 M_{\mathrm{N}}}\right)\left(\frac{\rho_{\mathrm{O}}}{10^3 M_{\mathrm{O}}}\right)\left(\frac{\rho_{\mathrm{O_2}}}{10^3 M_{\mathrm{O_2}}}+\frac{\rho_{\mathrm{N_2}}}{10^3 M_{\mathrm{N_2}}}\right),$$

$$R_{b7} = 10^3 k_{b7}\left(\frac{\rho_{\mathrm{NO}}}{10^3 M_{\mathrm{NO}}}\right)\left(\frac{\rho_{\mathrm{N}}}{10^3 M_{\mathrm{N}}}\right),$$

$$R_{b8} = 10^3 k_{b8}\left(\frac{\rho_{\mathrm{O_2}}}{10^3 M_{\mathrm{O_2}}}\right)\left(\frac{\rho_{\mathrm{N}}}{10^3 M_{\mathrm{N}}}\right),$$

where M_s is defined in grams. The species reaction rates are then expressed as:

$$\begin{aligned}
\dot{\omega}_{\mathrm{O}} &= M_{\mathrm{O}}\big[2(R_{f3}-R_{b3})+2(R_{f4}-R_{b4})+(R_{f5}-R_{b5})\\
&\qquad +(R_{f6}-R_{b6})-(R_{f7}-R_{b7})-(R_{f8}-R_{b8})\big],\\
\dot{\omega}_{\mathrm{O_2}} &= M_{\mathrm{O_2}}\big[-(R_{f3}-R_{b3})-(R_{f4}-R_{b4})+(R_{f8}-R_{b8})\big],\\
\dot{\omega}_{\mathrm{N}} &= M_{\mathrm{N}}\big[2(R_{f1}-R_{b1})+2(R_{f2}-R_{b2})+(R_{f5}-R_{b5})\\
&\qquad +(R_{f6}-R_{b6})+(R_{f7}-R_{b7})+(R_{f8}-R_{b8})\big],\\
\dot{\omega}_{\mathrm{N_2}} &= M_{\mathrm{N_2}}\big[-(R_{f1}-R_{b1})-(R_{f2}-R_{b2})-(R_{f7}-R_{b7})\big],\\
\dot{\omega}_{\mathrm{NO}} &= M_{\mathrm{NO}}\big[-(R_{f5}-R_{b5})\\
&\qquad -(R_{f6}-R_{b6})+(R_{f7}-R_{b7})-(R_{f8}-R_{b8})\big],
\end{aligned}$$

where M_s is defined in grams.

Appendix C: Thermal Kinetic Model

The vibrational relaxation was evaluated using coefficients from Ref. 18. These are given in Table X.

TABLE X: Vibrational relaxation coefficients used in Eq. 32 adopted from Ref. 18.

Species	A	B				
		O	O_2	N	N_2	NO
O_2	129	0.0271	0.0300	0.0265	0.0295	0.0298
N_2	220	0.0268	0.0295	0.0262	0.0290	0.0293
NO	168	0.0270	0.0298	0.0264	0.0293	0.0295

[1] P. S. Volpiani, "Numerical Strategy To Perform Direct Numerical Simulations of Hypersonic Shock/Boundary-Layer Interaction In Chemical Nonequilibrium," Shock Waves **31**, 361–378 (2021).

[2] C. T. Williams, M. D. Renzo, and P. Moin, "Turbulence–chemistry interaction in a non-equilibrium hypersonic boundary layer," Journal of Fluid Mechanics **1017**, A30 (2025).

[3] D. Passiatore, X. Gloerfelt, L. Sciacovelli, G. Pascazio, and P. Cinnella, "Direct numerical simulation of subharmonic second-mode breakdown in hypersonic boundary layers with finite-rate chemistry," International Journal of Heat and Fluid Flow **109**, 109505 (2024).

[4] D. Passiatore, L. Sciacovelli, P. Cinnella, and G. Pascazio, "Thermochemical Non-Equilibrium Effects In Turbulent Hypersonic Boundary Layers," Journal of Fluid Mechanics **941**, A21 (2022).

[5] D. Passiatore, L. Sciacovelli, P. Cinnella, and G. Pascazio, "Shock Impingement on a Transitional Hypersonic High-Enthalpy Boundary Layer," Physical Review Fluids **8**, 044601 (2023).

[6] P. P. Kerkar and S. Ghosh, "DNS of High-Enthalpy Effects On Turbulent Flows," in *AIAA Scitech 2019 Forum* (American Institute of Aeronautics and Astronautics Inc. (AIAA), 2019).

[7] S. Khurshid and D. A. Donzis, "Decaying Compressible Turbulence With Thermal Non-Equilibrium," Physics of Fluids **31**, 015103 (2019).

[8] A. G. Neville, I. Nompelis, P. K. Subbareddy, and G. V. Candler, "Thermal Non-Equilibrium Effects In Turbulent Compressible Shear Flows," in *45th AIAA Fluid Dynamics Conference* (American Institute of Aeronautics and Astronautics Inc. (AIAA), 2015).

[9] R. Fiévet, S. Voelkel, V. Raman, and P. L. Varghese, "Numerical Investigation of The Coupling of Vibrational Nonequilibrium and Turbulent Mixing Using State-Specific Description," Physical Review Fluids **4**, 013401 (2019).

[10] S. Lele, "Direct Numerical Simulation of Compressible Free Shear Flows," (1989), 10.2514/6.1989-374.

[11] M. M. Rogers and R. D. Moser, "The three-dimensional evolution of a plane mixing layer: the Kelvin–Helmholtz rollup," Journal of Fluid Mechanics **243**, 183–226 (1992).

[12] M. M. Rogers and R. D. Moser, "Direct Simulation of a Self-similar Turbulent Mixing Layer," Physics of Fluids **6**, 903–923 (1994).

[13] A. W. Vreman, N. D. Sandham, and K. H. Luo, "Compressible Mixing Layer Growth Rate and Turbulence Characteristics," Journal of Fluid Mechanics **320**, 235–258 (1996).

[14] J. H. Chen, "The Effect of Compressibility on Conserved Scalar Entrainment in a Plane Free Shear Layer," in *Turbulent Shear Flows 8* (Springer, Berlin, Heidelberg, 1993) pp. 297–311.

[15] X. Wang, J. Guo, J. Wang, and S. Chen, "Interfaces of High- and Low-Speed Large-Scale Structures in Compressible Turbulent Mixing Layers: Compressibility Effects and Structures," Journal of Fluid Mechanics **981** (2024), 10.1017/JFM.2024.55.

[16] D. Zhang, J. Tan, and X. Yao, "Direct Numerical Simulation of Spatially Developing Highly Compressible Mixing Layer: Structural Evolution and Turbulent Statistics," Physics of Fluids **31**, 36102 (2019).

[17] R. Boukharfane, P. J. M. Ferrer, A. Mura, and V. Giovangigli, "On the role of bulk viscosity in compressible reactive shear layer developments," European Journal of Mechanics - B/Fluids **77**, 32–47 (2019).

[18] P. A. Gnoffo, R. N. Gupta, and J. L. Shinn, "Conservation Equations and Physical Models For Hypersonic Air Flows In Thermal and Chemical Nonequilibrium," Tech. Rep. 2867 (National Aeronautics and Space Administration (NASA), 1989).

[19] J. H. Lee, "Basic Governing Equations for the Flight Regimes of Aeroassisted Orbital Transfer Vehicles," in *19th Thermophysics Conference* (American Institute of Aeronautics and Astronautics Inc. (AIAA), Reston, Virigina, 1984).

[20] C. Williams, M. Di Renzo, and J. Urzay, "Two-temperature Extension of the HTR Solver for Hypersonic Turbulent Flows in Thermochemical Nonequilibrium," Tech. Rep. (Center for Turbulence Research Annual Research Briefs, 2021).

[21] C. T. Williams, M. Di Renzo, and P. Moin, "Computational Framework for Direct Numerical Simulation of Shock-turbulence Interaction in Thermochemical Nonequilibrium," Tech. Rep. (Stanford.edu, 2022).

[22] V. Casseau, R. C. Palharini, T. J. Scanlon, and R. E. Brown, "A Two-Temperature Open-Source CFD Model For Hypersonic Reacting Flows, Part One: Zero-Dimensional Analysis," Aerospace **3**, 34 (2016).

[23] A. K. Chinnappan and M. Kim, "Species-Specific Vibrational Energy Model for Hypersonic Flow Simulations," (2025).

[24] D. A. Andrienko and I. D. Boyd, "Vibrational energy transfer and dissociation in O2-N2 collisions at hyperthermal temperatures," Journal of Chemical Physics **148** (2018), 10.1063/1.5007069/196551.

[25] J. W. Streicher, A. Krish, and R. K. Hanson, "Vibrational relaxation time measurements in shock-heated oxygen and air from 2000 K to 9000 K using ultraviolet laser absorption," Physics of Fluids **32**, 86101 (2020).

[26] J. W. Streicher, A. Krish, and R. K. Hanson, "Coupled vibration-dissociation time-histories and rate measurements in shock-heated, nondilute O2and O2-Ar mixtures from 6000 to 14 000 K," Physics of Fluids **33** (2021), 10.1063/5.0048059/1077260.

[27] J. W. Streicher, A. Krish, R. K. Hanson, K. M. Hanquist, R. S. Chaudhry, and I. D. Boyd, "Shock-tube measurements of coupled vibration-dissociation time-histories and rate parameters in oxygen and argon mixtures from 5000 K to 10 000 K," Physics of Fluids **32** (2020), 10.1063/5.0012426/1065419.

[28] J. W. Streicher, A. Krish, and R. K. Hanson, "Shock-Tube Measurements of Vibrational Relaxation Times In Oxygen and Nitrogen Mixtures Using Ultraviolet Laser Absorption Spectroscopy," in *AIAA Scitech 2020 Forum*, Vol. 1 PartF (American Institute of Aeronautics and Astronautics Inc. (AIAA), Reston, Virginia, 2020).

[29] G. V. Candler and I. Nompelis, "Computational Fluid Dynamics for Atmospheric Entry," Tech. Rep. (University of Minnesota, Minnesota, 2009).

[30] J. J. S. Shang, *Classic and High-Enthalpy Hypersonic Flows*, 1st ed. (CRC Press, 2023) p. 309.

[31] B. J. Mcbride, M. J. Zehe, and S. Gordon, "NASA Glenn Coefficients for Calculating Thermodynamic Properties of Individual Species," Tech. Rep. (National Aeronautics and Space Administration (NASA), 2002).

[32] J. O. Hirschfelder, C. F. Curtiss, and R. B. Bird, *Molecular Theory of Gases and Liquids* (John Wiley & Sons Inc, 1954) p. 1280.

[33] S. Chapman and T. G. Cowling, *Thermal Conduction and Diffusion in Gases* (Cambridge University Press, 1970).

[34] J. M. Yos, "Transport Properties of Nitrogen, Hydrogen, Oxygen, and Air to 30,000 K," Tech. Rep. (Massachusetts, 1963).

[35] J. M. Yos, "Approximate Equations for the Viscosity and Translational Thermal Conductivity of Gas Mixtures," Tech. Rep. (Contract Report No. AVSSD-0112-67-RM, Avco Corporation, Wilmington, Massachusetts, 1967).

[36] R. N. Gupta, J. M. Yos, R. A. Thompson, and K.-P. Lee, "A Review of Reaction Rates and Thermodynamic and Transport Properties for an 11-Species Air Model for Chemical and Thermal Nonequilibrium Calculations to 30000 K," Tech. Rep. (National Aeronautics and Space Administration (NASA), 1990).

[37]C. R. Wilke, "A Viscosity Equation for Gas Mixtures," The Journal of Chemical Physics **18**, 517–519 (1950).
[38]B. F. Armaly and K. Sutton, "Viscosity of multicomponent partially ionized gas mixtures," (1980).
[39]G. E. Palmer and M. J. Wright, "Comparison of Methods to Compute High-Temperature Gas Viscosity," Journal of Thermophysics and Heat Transfer **17**, 232–239 (2003).
[40]G. Palmer and M. J. Wright, "A Comparison of Methods to Compute High Temperature Gas Thermal Conductivity," 36th AIAA Thermophysics Conference (2003), 10.2514/6.2003-3913.
[41]A. Musawi and N. D. Sandham, "Efficient Viscosity and Thermal Conductivity Formulation for Scale-Resolved Hypersonic Flow Simulations," American Institute of Aeronautics and Astronautics **63** (2025).
[42]J. D. Ramshaw and C. H. Chang, "Friction-Weighted Self-Consistent Effective Binary Diffusion Approximation," Journal of Non-Equilibrium Thermodynamics **21**, 223–232 (1996).
[43]J.-H. Lee, "Basic Governing Equations for the Flight Regimes of Aeroassisted Orbital Transfer Vehicles," in *Thermal Design of Aeroassisted Orbital Transfer Vehicles*, Vol. 96, edited by H. F. Nelson (American Institute of Aeronautics and Astronautics, 1985) pp. 3–53.
[44]T. Poinsot and D. Veynante, *Theoretical and Numerical Combustion*, 2nd ed. (Edwards, 2005) p. 522.
[45]V. Giovangigli, "Transport Coefficients," in *Multicomponent Flow Modeling* (Birkhäuser, Boston, MA, 1999) pp. 97–117.
[46]K. Sutton and P. A. Gnoffo, "Multi-component diffusion with application to computational aerothermodynamics," in *7th AIAA/ASME Joint Thermophysics and Heat Transfer Conference* (American Institute of Aeronautics and Astronautics Inc, AIAA, 1998).
[47]E. Kustova, M. Mekhonoshina, A. Bechina, S. Lagutin, and Y. Voroshilova, "Continuum Models for Bulk Viscosity and Relaxation in Polyatomic Gases," Fluids 2023, Vol. 8, Page 48 **8**, 48 (2023).
[48]D. Bruno and V. Giovangigli, "Relaxation of internal temperature and volume viscosity," Physics of Fluids **23**, 93104 (2011).
[49]E. Kustova, R. Kumar, M. Massoudi, D. Bruno, and V. Giovangigli, "Internal Energy Relaxation Processes and Bulk Viscosities in Fluids," Fluids 2022, Vol. 7, Page 356 **7**, 356 (2022).
[50]M. S. Cramer, "Numerical estimates for the bulk viscosity of ideal gases," Physics of Fluids **24**, 66102 (2012).
[51]J. B. Freund, S. K. Lele, and P. Moin, "Compressibility effects in a turbulent annular mixing layer. Part 1. Turbulence and growth rate," Journal of Fluid Mechanics **421**, 229–267 (2000).
[52]W. G. Vincenti and C. H. Kruger, *Introduction to Physical Gas Dynamics* (Wiley, New York,, 1965) pp. xvii, 538 pages.
[53]C. Park, "On Convergence of Computation of Chemically Reacting Flows," in *AlAA 23rd Aerospace Sciences Meeting, 1985* (American Institute of Aeronautics and Astronautics Inc. (AIAA), 1985).
[54]C. Park, "Assessment of Two-Temperature Kinetic Model For Ionizing Air," in *Journal of Thermophysics and Heat Transfer*, Vol. 3 (American Institute of Aeronautics and Astronautics Inc. (AIAA), 1987) pp. 233–244.
[55]C. Park, "A Review of Reaction Rates In High Temperature Air," in *AIAA 24th Thermophysics Conference* (American Institute of Aeronautics and Astronautics Inc. (AIAA), 1989).
[56]C. Park, "Review of Chemical-Kinetic Problems of Future NASA Missions, I: Earth Entries," in *Journal of Thermophysics and Heat Transfer*, Vol. 7 (American Institute of Aeronautics and Astronautics Inc. (AIAA), 1993) pp. 385–398.
[57]C. Park, J. T. Howe, R. L. Jaffe, and G. V. Candler, "Review of Chemical-Kinetic Problems of Future NASA Missions, II: Mars Entries," in *Journal of Thermophysics and Heat Transfer*, Vol. 8 (American Institute of Aeronautics and Astronautics Inc. (AIAA), 1994) pp. 9–23.
[58]C. Park, R. L. Jaffe, and H. Partridge, "Chemical-Kinetic Parameters of Hyperbolic Earth Entry," Journal of Thermophysics and Heat Transfer **15**, 76–90 (2001).
[59]C. Park, "Assessment of A Two-Temperature Kinetic Model For Dissociating and Weakly Ionizing Nitrogen," in *Journal of Thermophysics and Heat Transfer*, Vol. 2 (American Institute of Aeronautics and Astronautics Inc. (AIAA), 1988) pp. 8–16.
[60]C. O. Johnston and A. M. Brandis, "Modeling of Nonequilibrium CO Fourth-Positive and CN Violet Emission In CO2-N2 Gases," Journal of Quantitative Spectroscopy and Radiative Transfer **149**, 303–317 (2014).
[61]R. L. Jaffe, D. W. Schwenke, G. M. Chaban, D. K. Prabhu, C. O. Johnston, and M. Panesi, "On The Development of A New Nonequilibrium Chemistry Model For Mars Entry," in *AIAA SciTech Forum - 55th AIAA Aerospace Sciences Meeting* (American Institute of Aeronautics and Astronautics Inc. (AIAA), 2017).
[62]C. Park, "Problems of Rate Chemistry In The Flight Regimes Of Aeroassisted Orbital Transfer Vehicles," in *AIAA Paper* (American Institute of Aeronautics and Astronautics Inc. (AIAA), 1984).
[63]C. Park, "Assessment of Two-Temperature Kinetic Model For Dissociating and Weakly-Ionizing Nitrogen," in *AIAA/ASME 4th Joint Thermophysics and Heat Transfer Conference* (American Institute of Aeronautics and Astronautics Inc. (AIAA), 1986).
[64]V. Casseau, *An Open-Source CFD Solver For Planetary Entry*, Ph.D. thesis, University of Strathclyde (2017).
[65]L. Landau and E. Teller, "Systematics of Vibrational Relaxation," Physik Zeitschrift der Sowjetunion **10**, 34–38 (1936).
[66]R. C. Millikan and D. R. White, "Systematics of Vibrational Relaxation," The Journal of Chemical Physics **39**, 3209–3213 (1963).
[67]F. Miró Miró, E. S. Beyak, F. Pinna, and H. L. Reed, "High-enthalpy models for boundary-layer stability and transition," Physics of Fluids **31** (2019), 10.1063/1.5084235.
[68]A. J. Smits and J. P. Dussauge, *Turbulent Shear Layers in Supersonic Flow: Second Edition*, 2nd ed. (Springer New York, 2006) pp. 1–410.
[69]B. E. Launder and N. D. Sandham, *Closure Strategies for Turbulent and Transitional Flows*, edited by B. E. Launder and N. D. Sandham (Cambridge University Press, 2002).
[70]D. J. Lusher, S. P. Jammy, and N. D. Sandham, "OpenSBLI: Automated Code-Generation for Heterogeneous Computing Architectures Applied to Compressible Fluid Dynamics on Structured Grids," Computer Physics Communications **267**, 108063 (2021).
[71]D. J. Lusher, A. Sansica, N. D. Sandham, J. Meng, B. Siklósi, and A. Hashimoto, "OpenSBLI v3.0: High-Fidelity Multi-Block Transonic Aerofoil CFD Simulations Using Domain Specific Languages on GPUs," Computer Physics Communications **307**, 109406 (2025).
[72]B. R. Ramaprian, . N. D. Sandham, . M. G. Mungal, . W. C. Reynolds, N. D. Sandham, M. G. Mungal, and W. C. Reynolds, "Passive scalar tagging for the study of coherent structures in the plane mixing layer," Physics of Fluids A: Fluid Dynamics **1**, 2034–2041 (1989).
[73]N. D. Sandham and W. C. Reynolds, "Three-dimensional simulations of large eddies in the compressible mixing layer," Journal of Fluid Mechanics **224**, 133–158 (1991).
[74]P. Moin, A. Leonard, and J. Kim, "Evolution of a curved vortex filament into a vortex ring," The Physics of Fluids **29**, 955–963 (1986).
[75]C. Pantano and S. Sarkar, "A study of compressibility effects in the high-speed turbulent shear layer using direct simulation," Journal of Fluid Mechanics **451**, 329–371 (2002).
[76]T. J. Fuller, A. G. Hsu, R. Sanchez-Gonzalez, J. C. Dean, S. W. North, and R. D. Bowersox, "Radiofrequency plasma stabilization of a low-Reynolds-number channel flow," Journal of Fluid Mechanics **748**, 663–691 (2014).